ACS Catalysis

Research Article

pubs.acs.org/acscatalysis

Local Platinum Environments in a Solid Analogue of the Molecular Periana Catalyst

Mario Soorholtz,[†,¶,▽] Louis C. Jones,[‡,¶] Dominik Samuelis,[§] Claudia Weidenthaler,[†] Robin J. White,[∥,○] Maria-Magdalena Titirici,[∥,◆] David A. Cullen,[⊥] Tobias Zimmermann,[†] Markus Antonietti,[∥] Joachim Maier,[§] Regina Palkovits,[†,#] Bradley F. Chmelka,[*,‡] and Ferdi Schüth[*,†]

[†]Max-Plank-Institut für Kohlenforschung, Mülheim an der Ruhr, D-45470, Germany

[‡]Department of Chemical Engineering, University of California, Santa Barbara, California 93106-5080, United States

[§]Max Planck Institute for Solid State Research, Stuttgart, D-70569, Germany

[∥]Max Planck Institute of Colloids and Interfaces, Potsdam, D-14476, Germany

[⊥]Oak Ridge National Laboratory, Oak Ridge, Tennessee 37831, United States

[#]RWTH Aachen University, Aachen, D-52074, Germany

Supporting Information

ABSTRACT: Combining advantages of homogeneous and heterogeneous catalysis by incorporating active species on a solid support is often an effective strategy for improving overall catalyst performance, although the influences of the support are generally challenging to establish, especially at a molecular level. Here, we report the local compositions, and structures of platinum species incorporated into covalent triazine framework (Pt-CTF) materials, a solid analogue of the molecular Periana catalyst, $Pt(bpym)Cl_2$, both of which are active for the selective oxidation of methane in the presence of concentrated sulfuric acid. By using a combination of solid-state ^{195}Pt nuclear magnetic resonance (NMR) spectroscopy, aberration-corrected scanning transmission electron microscopy (AC-STEM), X-ray photoelectron spectroscopy (XPS), and X-ray absorption spectroscopy (XAS), important similarities and differences are observed between the Pt-CTF and Periana catalysts, which are likely related to their respective macroscopic reaction properties. In particular, wide-line solid-state ^{195}Pt NMR spectra enable direct measurement, identification, and quantification of distinct platinum species in as-synthesized and used Pt-CTF catalysts. The results indicate that locally ordered and disordered Pt sites are present in as-synthesized Pt-CTF, with the former being similar to one of the two crystallographically distinct Pt sites in crystalline $Pt(bpym)Cl_2$. A distribution of relatively disordered Pt moieties is also present in the used catalyst, among which are the principal active sites. Similarly XAS shows good agreement between the measured data of Pt-CTF and a theoretical model based on $Pt(bpym)Cl_2$. Analyses of the absorption spectra of Pt-CTF used for methane oxidation suggests ligand exchange, as predicted for the molecular catalyst. XPS analyses of $Pt(bpym)Cl_2$, Pt-CTF, as well as the unmodified ligands, further corroborate platinum coordination by pyridinic N atoms. Aberration-corrected high-angle annular dark-field STEM proves that Pt atoms are distributed within Pt-CTF before and after catalysis. The overall results establish the close similarities of Pt-CTF and the molecular Periana catalyst $Pt(bpym)Cl_2$, along with differences that account for their respective properties.

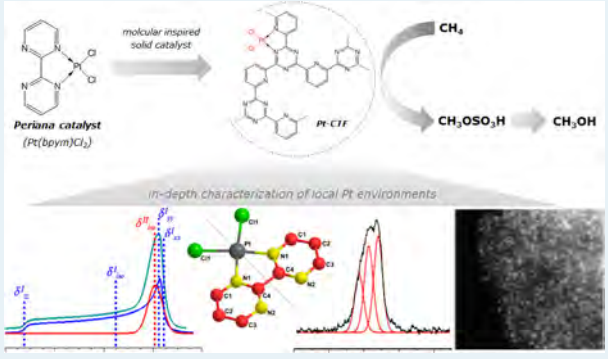

KEYWORDS: *methane oxidation, Periana catalyst, solid analogue vs molecular catalyst, solid-state ^{195}Pt NMR, atomic dispersion*

1. INTRODUCTION

Solid catalysts functionalized with molecular metal complexes have the potential to bridge the gap between heterogeneous and homogeneous catalysis by combining the advantages of both. These include facile catalyst separation from reacting fluids and relatively uniform distributions of well-defined active sites.[1−3] In contrast, commonly used solid catalysts, such as supported metals or metal oxides, typically exhibit heterogeneous distributions and environments of active sites with diverse energetics and reactivities.[4] By comparison, the well-defined nature of active sites in homogeneous molecular complexes can provide guidance for the modification of catalyst properties and performances by grafting transition-metal complexes onto solid surfaces. Similar heterogenized catalysts can be synthesized by chemically modifying molecular complexes, so that they form extended solid analogues of

Received: October 14, 2015
Revised: January 14, 2016

DOI: 10.1021/acscatal.5b02305
ACS Catal. 2016, 6, 2332−2340

Scheme 1. Schematic Diagram for the Synthesis of the Pt-CTF Catalyst[a]

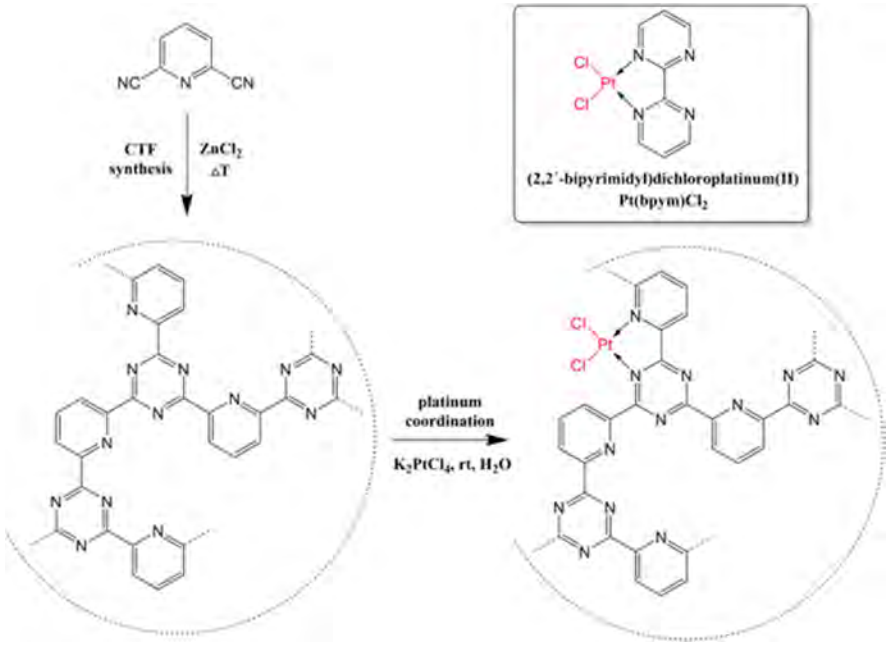

[a]Aromatic dinitrile (i.e., 2,6-dicyanopyridine) is converted via ionothermal polymerization in molten $ZnCl_2$ (step 1:400 °C, 40 h; step 2:600 °C, 40 h) into an extended nitrogen-rich polymeric scaffold (covalent triazine framework, CTF). A simple coordination approach, including the addition of CTF to an aqueous solution containing the Pt^{II} precursor ions, results in a Pt-modified CTF network containing moieties that resemble the molecular $Pt(bpym)Cl_2$ catalyst (upper right). The schematic CTF structures shown are idealized, as the high polymerization temperatures lead to some nonstoichiometric modifications of the polymeric scaffold.

their homogeneous counterparts. Such materials are invariably accompanied by the challenges of identifying and characterizing the catalytically active sites and their environments within the solid scaffold at the molecular level. Thomas et al. have described various characterization techniques for such materials that are capable of providing valuable atomic-scale information,[5,6] although subtle differences between the molecular complexes on different support materials have been challenging to measure and difficult to distinguish.

Over the past decades, many synthesis strategies have been developed to enable the incorporation of molecular catalysts onto or into solid supports. For example, Maschmeyer et al.,[7] Jarupatrakorn et al.,[8] Thomas et al.,[6] and Corma,[9] have reported synthesis procedures that selectively modify the surface of silica materials with single transition-metal atoms in defined environments. Isomorphous substitution of four-coordinate Ti^{IV} atoms for Si^{IV} atoms in microporous, crystalline zeolite frameworks (i.e., TS-1) has been shown to yield isolated Ti centers, that exhibit high activities for catalytic oxidation that are now being used industrially.[10] In contrast to inorganic supports, however, porous organic polymers and carbons have received relatively little attention in the literature. Corma et al.[11] and McNamara et al.[12] have reviewed several approaches to heterogenize molecular complexes within polymeric scaffolds. A promising alternative is the design of a stable solid framework that contains ligand motifs as an integral part of the framework. To these ligand motifs, atomically dispersed metal centers can be coordinated, yielding solid analogues of molecular catalysts, which is the focus of this study. Independent of whether the heterogenized catalysts are based on inorganic or polymeric networks, the local environments of the metal centers have been difficult to measure and correlate with their catalytic activities, because of the lack of long- and often short-range atomic order.

Here, the local compositions, structures and distributions of Pt species are quantitatively established for a novel solid mimic of the Periana catalyst, i.e., η^2-(2,2′-bipyrimidyl)-dichloroplatinum(II) ($Pt(bpym)Cl_2$), a well-known molecular catalyst. Periana et al. demonstrated that the molecular catalyst is active and selective for the partial oxidation of methane via C−H activation in fuming sulfuric acid.[13,14] By comparison, in the heterogenized catalyst, Pt^{II}−Cl_2 species are coordinated to a nitrogen-rich triazine polymeric network, referred to here as a "covalent triazine framework" (CTF), the polymer building unit of which resembles the 2,2′-bipyrimidine ligand of its molecular counterpart (Scheme 1). Microporous CTFs (without coordinated metal atoms) have previously been reported by Kuhn et al., who used the trimerization of an aromatic dinitrile under ionothermal conditions at temperatures of up to 600 °C.[15,16] For the synthesis of the Pt-modified CTF catalyst (Pt-CTF) we report here, Pt atoms were introduced via a simple coordination approach in water at room temperature using K_2PtCl_4 as a platinum source. The catalytic properties of Pt-CTF for selective partial oxidation of methane to methanol (via methylbisulfate) under extremely harsh reaction conditions (i.e., 215 °C, 90 bar CH_4, oleum (30 wt % SO_3)) were recently reported in a short communication.[17] In particular, measured turnover numbers (TONs) were stable for at least six subsequent runs. In a follow-up study, Pt-CTF proved to be somewhat less active (TOF = 174 h^{-1}) than its molecular counterpart $Pt(bpym)Cl_2$ (TOF = 912 h^{-1}),[18] which is a commonly observed tradeoff for the added benefits of heterogenized catalysts. The catalytic performance of the solid Pt-CTF catalyst was found to be very promising, although

DOI: 10.1021/acscatal.5b02305
ACS Catal. 2016, 6, 2332−2340

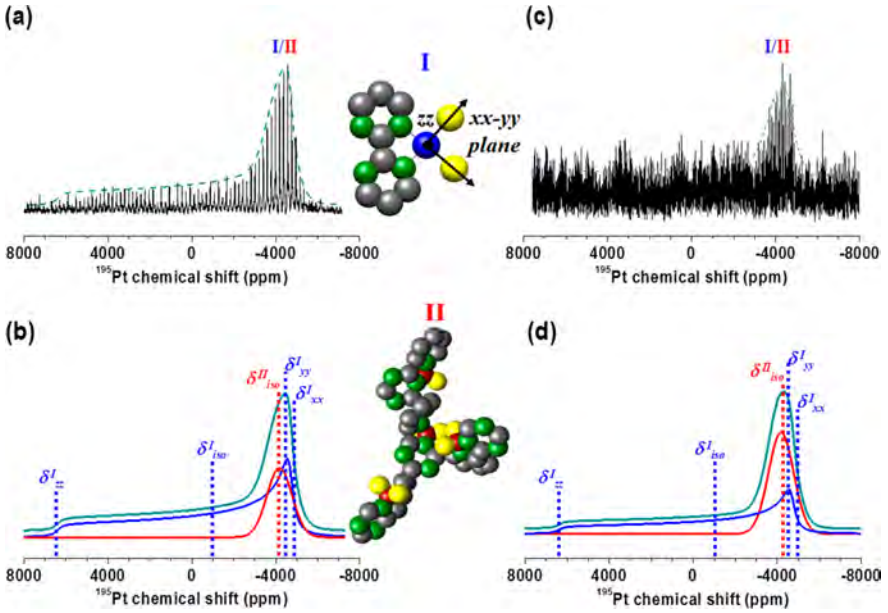

Figure 1. Static solid-state ^{195}Pt WURST-CPMG NMR spectra (black) of Pt-CTF: (a) as-synthesized before and (c) after use under reaction conditions of 215 °C, 90 bar CH_4, and oleum (20 wt % SO_3) for 2.5 h. (b, d) Summed line shape fits (green lines) of deconvoluted spectral components from two different types of ^{195}Pt sites in the experimental spectra: a locally ordered axially symmetric ^{195}Pt site (blue, 75% ± 10%) and a distribution of relatively disordered ^{195}Pt moieties (red, 25% ± 10%) (panel b); and a similar axially symmetric site (53% ± 10%) and similarly disordered ^{195}Pt moieties (47% ± 10%), as present in the as-synthesized Pt-CTF material (panel (b)), but with different population distributions (panel (d)). Proposed local structures of the different types of ^{195}Pt sites (I, blue; II, red) are shown as insets, with N atoms shown in green, C atoms shown in gray, and Cl atoms shown in yellow. Identical CSA and Gaussian line shape parameters were used to fit the signals associated with ^{195}Pt sites I and sites II, respectively. Chemical shift parameters (δ_{xx}, δ_{yy}, δ_{zz}, and δ_{iso}) are orientation-specific descriptors of the local ^{195}Pt bonding environments and are indicated for each line shape in panels (b) and (d), with values tabulated in the Supporting Information (Tables S1 and S2). Axes shown for site I indicate the directions of the principal components (δ_{xx}, δ_{yy}, δ_{zz}) of the chemical shift tensor.

the nature(s) of the platinum sites and their comparisons to the molecular Periana catalyst have thus far remained unknown.

Nevertheless, by using state-of-the-art solid-state ^{195}Pt nuclear magnetic resonance (NMR) measurements, in conjunction with results from X-ray photoelectron spectroscopy (XPS), X-ray absorption spectroscopy (XAS), aberration-corrected scanning transmission electron microscopy (STEM), and structural modeling, detailed information is obtained on the types, relative populations, and local structural environments of distinct Pt species within the Pt-CTF catalyst. The analyses provide unprecedented insights into the nature(s) of molecular Pt sites in a heterogeneous catalyst, specifically a solid-state analogue of the Periana catalyst that promotes activity for the selective partial oxidation of methane.

2. RESULTS AND DISCUSSION

2.1. Direct Measurements of Molecular Pt Environments. The molecular similarities and differences between Pt sites in the solid Pt-CTF catalyst before and after use under catalytic reaction conditions are established by using solid-state ^{195}Pt NMR spectroscopy to probe the local bonding environments of ^{195}Pt atoms directly. Recently, Schurko and coworkers have demonstrated the effectiveness of low-power frequency sweeps to acquire ultrabroad NMR spectra (by using the technique of Wideband Uniform-Rate Smooth-Truncation Carr−Purcell−Meiboom−Gill,[19,20] WURST-CPMG) that enable detailed molecular analyses and understanding of previously intractable materials. This includes the Pt-CTF catalyst considered here, whose molecular ^{195}Pt species were measured directly by acquiring static solid-state ^{195}Pt NMR spectra (Figure 1). The ultrabroad line widths (~10 000 ppm) of ^{195}Pt NMR signals render line-narrowing methods (e.g., magic-angle sample spinning) ineffective and instead require specialized frequency-sweep techniques, such as the WURST-CPMG method, to effectively excite the entire ^{195}Pt NMR spectrum.[21] This approach yields a series of time-domain signal echoes, which, after Fourier transformation, yield a corresponding series of spikelets in the frequency domain with an intensity manifold that reflects the overall line shape of a static ^{195}Pt NMR spectrum. All of the ^{195}Pt species measured in this study are expected to be diamagnetic, and thus have comparable and sufficiently long T_2 values (ca. 2 ms) to be suitable for the WURST-CPMG method.

Though lacking long-range atomic order (i.e., over dimensions greater than ~10 nm), as manifested by the absence of narrow X-ray reflections (Figure S1 in the Supporting Information), the solid-state ^{195}Pt NMR spectrum in Figure 1a clearly establishes that the Pt atoms in the Pt-CTF catalyst nevertheless exhibit relatively high extents of local (i.e., over dimensions of ~1 nm) structural order. The solid-state ^{195}Pt NMR spectrum in Figure 1a of Pt-CTF exhibits intensity in a range that is associated with diamagnetic ^{195}Pt species and consistent with the presence of molecular Pt complexes.[22] In addition, the overall intensity manifold (Figure 1a, dashed line) can be well-fitted by two overlapping lineshapes (Figure 1b) that manifest contributions from two distinct types of ^{195}Pt sites, one that is relatively ordered and dominant (blue, site I) and another that is more disordered (red, site II). The blue ^{195}Pt linefit is characteristic of an axially symmetric chemical-shift-anisotropy (CSA)[23] powder pattern that manifests a high degree of local bonding order. Furthermore, the singularities observed in this ^{195}Pt CSA line shape yield detailed quantitative

DOI: 10.1021/acscatal.5b02305
ACS Catal. 2016, 6, 2332−2340

information on the local bonding at ^{195}Pt site I, as characterized by the principal axes components of the ^{195}Pt chemical shift tensor (δ_{xx}, δ_{yy}, δ_{zz}), the isotropic ^{195}Pt chemical shift ($\delta_{iso} = (\delta_{xx} + \delta_{yy} + \delta_{zz})/3$), and anisotropy parameter ($\eta = (\delta_{yy} - \delta_{xx})/(\delta_{zz} - \delta_{iso})$). The respective fits in Figure 1b include an almost-axially symmetric ($\eta = 0.06$) line shape (site I) from a relatively locally ordered and predominant (ca. 75% ± 10%) type of ^{195}Pt site with CSA parameters (Table S1) that reflect approximately square-planar C_{2v} symmetry, as found in other crystalline Pt–N_xCl_y complexes.[22] In addition, both the asymmetry parameter ($\eta = 0.06$) and the correspondingly similar δ_{xx} and δ_{yy} values (−4900 and −4500 ppm, respectively) of the ^{195}Pt chemical shift tensor are comparable to the CSA parameters ($\eta = 0.04$, $\delta_{xx} = -4800$ ppm, $\delta_{yy} = -4600$ ppm) for one of the two distinct sites within the crystalline Pt(bpym)Cl_2 analogue (see Figure S2 and Table S3 in the Supporting Information). This site appears to correspond to one of two square-planar stacking motifs in the Pt(bpym)Cl_2 crystal (Figure S2b; site 1), whereby π–π stacking of the bipyrimidine moieties results in an almost-undistorted square-planar configuration of the associated Pt site.[24] Since ^{195}Pt is known to have an extremely broad chemical shift range, such similar tensor values indicate that the locally ordered ^{195}Pt site-I coordination environments in Pt-CTF are similar to those of site 1 in crystalline Pt(bpym)Cl_2, albeit dispersed within the CTF network without long-range atomic order. Such insights would not have been possible to obtain without the direct and quantitative analyses enabled by the ultrabroad solid-state ^{195}Pt NMR spectrum.

Interestingly, in addition to the similarities, there are also notable differences between the solid-state ^{195}Pt NMR spectra of the solid Pt-CTF catalyst and crystalline Pt(bpym)Cl_2. In particular, the z-components of their chemical shift tensors (δ_{zz}) are significantly different, 6400 ppm versus 1900 ppm, respectively (see Tables S1 and S3), manifesting distinct interactions normal to the square plane of the ^{195}Pt complexes. The observed displacement to higher frequency (larger ppm) for Pt-CTF is consistent with the greater influence of ring currents associated with the extended π-electron network[25] or shorter Pt–Cl and Pt–N bond distances.[23] In addition, there is evidence of a signal that is subtly visible as a manifold of broadened spikelets centered at −4200 ppm (Figure 1b, red), which coincide with the δ_{xx} and δ_{yy} ^{195}Pt chemical shift tensor values associated with both site I of Pt-CTF and site 1 of crystalline Pt(bpym)Cl_2, although it cannot be fit by a CSA powder pattern. However, this ^{195}Pt signal intensity can be taken into account by a Gaussian distribution (∼1400 ppm full width at half maximum (fwhm)) centered at −4200 ppm, which reflects a minority of Pt sites (site II, ca. 25% ± 10%). These sites possess a distribution of local ^{195}Pt environments that are distorted from a square-planar configuration, consistent with a distribution of nitrogenous-coordinating moieties within the branched and disordered CTF structure. (Based on a comparison of individually Fourier-transformed time-domain signal echoes, the ^{195}Pt spin–spin (T_2) relaxation times of sites I and II are similar (∼2 ms), so that their integrated ^{195}Pt signals are expected to yield reliable estimates of their relative populations.) Moreover, both types of ^{195}Pt sites in the Pt-CTF catalyst exhibit significantly shorter ^{195}Pt spin–lattice (T_1) relaxation times (ca. 0.5 s), compared to those associated with bulk crystalline Pt(bpym)Cl_2 (ca. 5.0 s). The shorter T_1 values are consistent with the lack of long-range molecular order in the Pt-CTF material manifested by the absence of wide-angle scattering reflections in the XRD pattern of the solid Pt-CTF material (Figure S1). The solid-state ^{195}Pt NMR spectra and spin-relaxation time measurements thus enable distinct types of locally ordered and disordered Pt environments to be distinguished and compared for the Pt-CTF catalyst.

Importantly, changes of the Pt moieties in Pt-CTF upon use as a catalyst for the selective oxidation of methane can be probed by comparing solid-state ^{195}Pt NMR spectra acquired before and after reaction at 215 °C and 90 bar CH_4 in oleum (20 wt % SO_3) for 2.5 h. In particular, the solid-state ^{195}Pt spectrum after reaction of the Pt-CTF catalyst (Figure 1c) shows notable similarities with, as well as several differences from, the as-synthesized material (Figure 1a). First, the signal-to-noise ratio (S/N) is notably lower (even after 4 days of measurement), reflecting a lower Pt content in the Pt-CTF catalyst after reaction. This is consistent with separate results that have demonstrated a stable loading of ∼5 wt % Pt for the reaction conditions used, with the balance being leached and lost (see Figure S3 and Table S4 in the Supporting Information). Based on the difference in platinum contents, ca. 36 days of measurement time would have been necessary to achieve an equivalent signal-to-nosie (S/N) ratio, which was infeasible to carry out. Normalizing the ^{195}Pt NMR spectra in Figures 1a and 1c, with respect to their respective mass% Pt, yields comparable signal intensities that account for their different platinum contents. Nevertheless, ^{195}Pt signal intensity is clearly visible at −4200 ppm (site II, ∼1500 ppm fwhm; see Figure 1c, as well as Table S2), with evidence of line shape asymmetry to higher frequency that indicates a contribution from chemical shift anisotropy and accounts for the weak spikelet intensity extending toward 7000 ppm (site I). For the spectra in Figures 1a and 1c, it is noteworthy that the spikelets that manifest the putative ^{195}Pt lineshapes are all separated by 200 ppm and can be distinguished by their periodicity. In Figure 1c, the spikelets are weaker, but periodic and clearly discernible above the noise of the spectrum in the region of the intensity maximum near −4200 ppm. In particular, the spikelet intensity manifold centered at approximately −4200 ppm is skewed to higher frequency, consistent with an axially symmetric spectral feature that is similar to that in Figure 1a. The spikelet manifold also manifests an underlying pattern that exhibits a Gaussian distribution of intensity that is similar to that in Figure 1a and was attributed to a distribution of relatively disordered Pt species (site II). This is consistent with the similar spikelet intensity observed over the same range, as discussed above for as-synthesized Pt-CTF (Figure 1a, Table S1) and for Pt(bpym)Cl_2 (Figure S2, Table S3). Within the sensitivity and resolution limits of the ^{195}Pt NMR measurements, these signals indicate very similar local Pt environments in the materials, with respect to the xx and yy (δ_{xx} and δ_{yy}) components of their ^{195}Pt chemical shift tensors and similar in-plane Pt bonding configurations with N and Cl atoms. Furthermore, this establishes that such Pt moieties, which are present in Pt-CTF before and after exposure to the harsh catalytic reaction conditions, are relatively stable against chemical modification. A comparison of the line shape fits in Figures 1b and 1d reveals that the relative integrated intensities associated with the different Pt sites reflect a larger proportion of partially disordered Pt moieties (site II) in the used Pt-CTF catalyst material. These observations suggest that Pt sites within this distribution of relatively disordered environments may be responsible for the measured catalytic activity.

Whether Pt(IV) has a prime role in the catalytic cycle, as recently suggested by Mironov et al. for the molecular system,[26]

DOI: 10.1021/acscatal.5b02305
ACS Catal. 2016, 6, 2332–2340

cannot be answered with these data and remains to be addressed in future studies. Overall, the solid-state ^{195}Pt NMR spectra provide detailed insights on the local compositions and structures of Pt moieties in the solid Pt-CTF and Periana catalysts, along with subtle molecular heterogeneities that are likely related to their methane oxidation reactivities.

The local structures of Pt moieties in Pt-CTF and crystalline Pt(bpym)Cl_2 are corroborated by extended X-ray absorption fine structure (EXAFS) and X-ray absorption near-edge structure (XANES) spectroscopy. EXAFS provides information on the average short-range structure of the Pt-CTF networks, allowing the determination of possible Pt coordination motifs within the amorphous polymeric scaffold (see Figure S1 for XRD patterns). Based on the quantitative solid-state ^{195}Pt NMR results, the predominant and relatively ordered square-planar Pt moiety (site I, accounting for ∼75% of the total signal) is expected to be the site to which EXAFS will be most sensitive. By comparison, XANES yields information on average Pt concentration (Table S5 in the Supporting Information) and on the average electron density for different Pt sites (Table 1, *vide infra*). The interpretation of the EXAFS region was supported by fitting with a theoretical structural model of Pt(bpym)Cl_2, the postulated molecular counterpart of Pt-CTF (Figure 2). Because of the short-range sensitivity of EXAFS, ∼3−4 coordination shells around the Pt atoms, good agreement between measured EXAFS spectra and theory would be expected for Pt-CTF structures that have the basic coordination motifs of the Pt(bpym)Cl_2 catalyst, especially for a first-coordination shell comprised of 2 Cl ligands and 2 N ligands.

Table 1. White-Line Positions in XANES Region for Reference Materials and Pt-CTF before and after Use as a Catalyst

material	white-line position (eV)
K_2PtCl_4	11565.46
Pt(bpym)Cl_2	11566.47
$PtCl_4$	11567.45
Pt-CTF before catalysis	11566.64
Pt-CTF after catalysis	11567.22

The structural model for Pt(bpym)Cl_2 (Figure 2a) exhibits similar atomic distances for Pt−N1, Pt−C4, Pt−C1, and Pt−Cl, which render a complex, first-coordination shell around the transition-metal atom (Figure 2b, blue curve). Accordingly, the Fourier-transformed $\chi(k)$ function of the measured Pt-CTF shows a broad overlapping signal for the first coordination shell (Figure 2b, red curve). EXAFS fits of the as-made Pt-CTF samples (Tables S6−S8 in the Supporting Information) with a structural model based on Pt(bpym)Cl_2 illustrate that all characteristics of the measured spectrum can be reproduced, an indication that the mean local environment(s) of Pt is similar in both cases. Fit quality is sufficiently good for an amorphous substance. Interatomic distances agree well with the Pt(bpym)-Cl_2 reference, except for being consistently ∼3%−4% shorter than in the model structure. Such shorter bond lengths are consistent with the differences in the respective δ_{zz} values of the ^{195}Pt chemical shift tensor for the Pt sites in Pt-CTF versus Pt(bpym)Cl_2 (see Figure 1, as well as Tables S1 and S3). Within detection limits of 5%−10%, no evidence for other ordered Pt coordination motifs could be found within Pt-CTF. Large variances (Debye−Waller factors (σ^2)), especially for higher coordination shells (Table S8), suggest that CTF exhibits a nonordered structure with varying Pt coordination, geometries, and distances between Pt sites and next-nearest neighbor C atoms within CTF, consistent with a minority of locally disordered Pt sites (∼25%) found using solid-state ^{195}Pt NMR. Stronger attenuation of multiple scattering paths, compared to the Pt(bpym)Cl_2 model, indicates a deviation from a fully planar structure. However, the Pt−Cl (and within error margins, the Pt−N1) bonds exhibit relatively small variances that can be explained by thermal motion, which suggests structural disorder is limited to the CTF network. In fact, the first-coordination shell closely resembles the model Pt(bpym)Cl_2 coordination motif. This was also established by the solid-state ^{195}Pt NMR, as well as the XRD results, which show the amorphous structure of as-synthesized Pt-CTF (Figure S1). Also XPS clearly shows variability of the nitrogen moieties present in Pt-CTF (Figure 3, *vide infra*). Furthermore, verification of bidentate Pt coordination in the Pt-CTF materials with various Pt contents (Table S5) showed that all spectra exhibit identical features, indicating macroscopically homogeneous Pt coordination within CTF at higher platinum contents (see Figures S4a−d).

Structural changes as a result of methane oxidation in hot oleum were established by *ex situ* EXAFS characterization of a Pt-CTF catalyst that had been exposed to reaction conditions (i.e., 2.5 h, 215 °C, oleum (20 wt % SO_3), 90 bar CH_4). A clearly visible shoulder at ∼2.3 Å (Figures 2c and 2d; red curve) is not reproduced in the fit with the Pt(bpym)Cl_2 structural model. In addition, EXAFS fit parameters give much higher S_0^2 values (i.e., >0.92, Table S6), which are not typical for polymeric materials, indicating that the mean Pt coordination environment was altered by the reaction conditions. Moreover, the σ^2 values significantly differ from the previous fits (Table S8), which is an additional indication that the local environment(s) of Pt atoms were altered during catalytic reaction. For the molecular catalyst, Kua et al.[28] concluded, based on DFT calculations, that one Cl ligand is irreversibly lost during the first turnover, accompanied by release of hydrochloric acid (HCl) and regeneration of the catalyst as Pt(bpym)Cl(HSO_4) or protonated forms. Recently, ligand exchange, although under different reaction conditions, was shown to happen in a Pt-modified metal organic framework with a similar Pt environment by means of EXAFS.[29] Accordingly, the structural model presented here was modified by replacing chloride with a bisulfate group to test this hypothesis for the solid Pt-CTF analogue. An overlay of Fourier-transformed $\chi(k)$ functions for the Pt(bpym)Cl(OSO_3H) model and for Pt-CTF (Figure 2d; blue and red curves, respectively) shows that the signal at ∼2.3 Å can be accounted for by this modified structural model. A refinement of first-coordination-shell atoms consistently yields a N:Cl:O ratio of ∼2:1:1 (±0.5) for a set of four Pt-CTF catalysts evaluated after exposure to identical reaction conditions (see Table S9 in the Supporting Information). Thus, the EXAFS data suggest that ligand exchange occurs during reaction at the transition-metal center within Pt-CTF, analogous to its molecular counterpart Pt(bpym)Cl_2. Changes in the mean electron density and oxidation state at the Pt sites before and after catalysis provide valuable information about potential structural alteration at the metal center. As-made and used samples of Pt-CTF were compared with respect to their white-line positions (Table 1) in the XANES region of the X-ray absorption spectra (XAS). The white-line position of Pt-CTF shifted by 0.58 eV to higher binding energies after the

DOI: 10.1021/acscatal.5b02305
ACS Catal. 2016, 6, 2332−2340

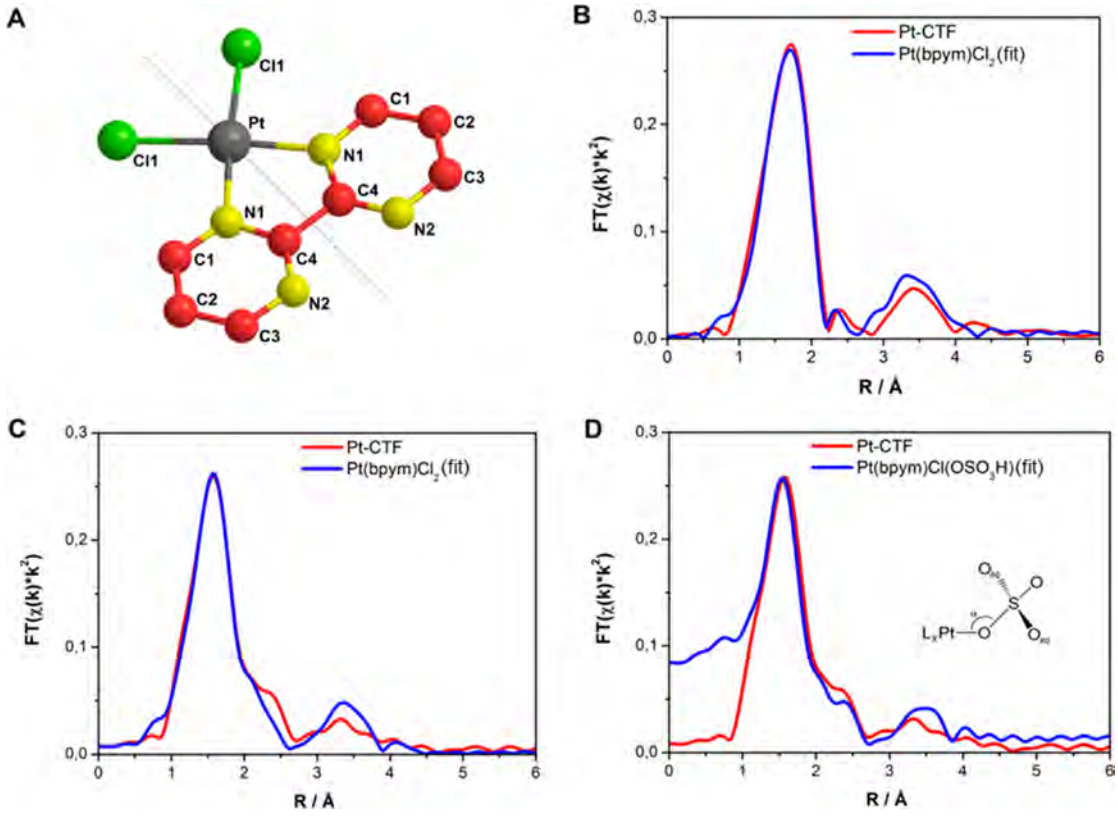

Figure 2. Extended X-ray absorption fine structure (EXAFS) analysis: (a) structural model of $Pt(bpym)Cl_2$ taken as a reference, using Cartesian coordinates from Xu et al.;[27] (b) Fourier transformed $\chi(k)$ functions of as-made Pt-CTF and the fitted theoretical $Pt(bpym)Cl_2$ model. Details for the fit parameters are given in the Supporting Information; (c, d) Fourier-transformed $\chi(k)$ functions of Pt-CTF after methane oxidation (2.5 h, 215 °C, oleum (20 wt % SO_3), 90 bar CH_4) (red) and the fitted theoretical model (blue) ($Pt(bpym)Cl_2$ model (panel (c)) and $Pt(bpym)Cl(OSO_3H)$ model (model shown as an inset) (panel (d))).

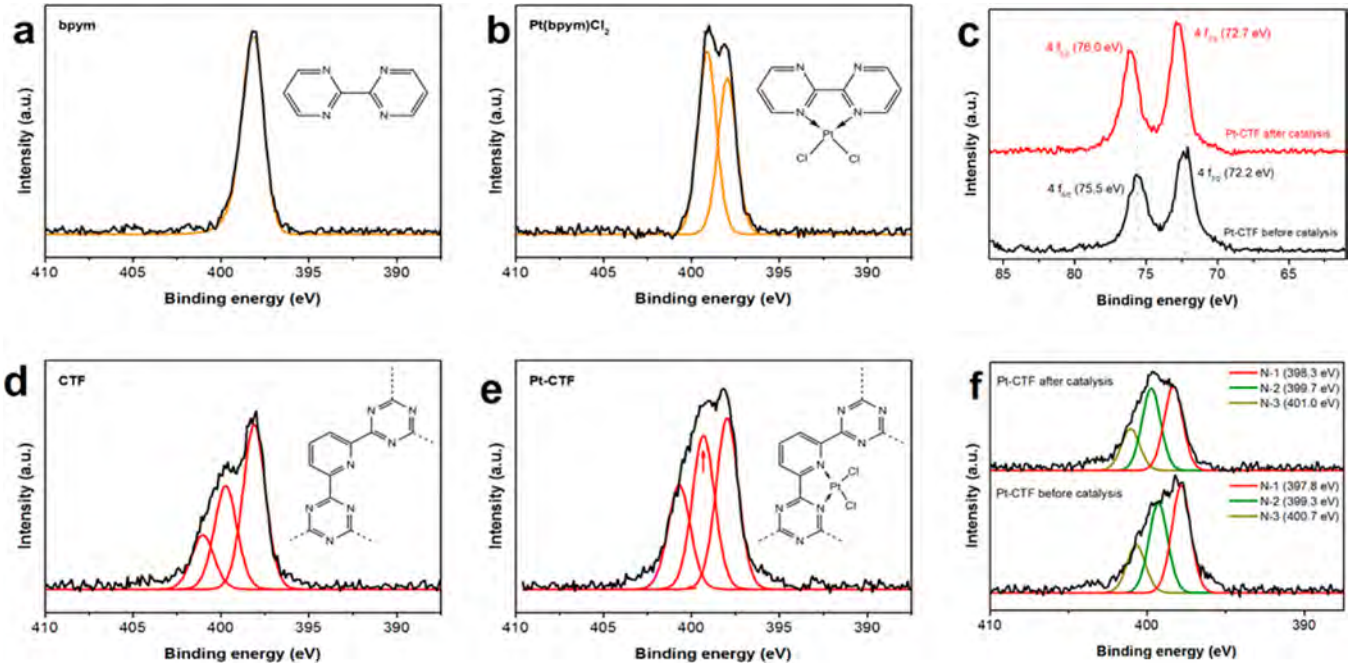

Figure 3. (a, d) XPS N 1s spectra of unmodified and (b, e) Pt-modified 2,2′-bypyrimidine ligand and CTF, respectively. Comparison between XPS (c) Pt 4f and (f) N 1s spectra for Pt-CTF before and after exposure to reaction conditions for the partial oxidation of methane (2.5 h, 215 °C, oleum (20 wt % SO_3), 90 bar CH_4).

catalyst had been tested under reaction conditions. A shift to higher binding energy indicates a decrease in the electron density at the Pt atom, consistent with ligand substitution by bisulfate anions, which are weakly coordinating and exhibit less

DOI: 10.1021/acscatal.5b02305
ACS Catal. 2016, 6, 2332−2340

donating ability. The combined XAS analysis indicates a high degree of similarity between Pt environments in Pt-CTF and the coordination motif of Pt(bpym)Cl_2. In addition, Pt-CTF undergoes structural changes during use in catalysis that correlate with intermediates previously postulated for its molecular counterpart.

Energies of the white-line center in the XANES spectra were determined by peak-fitting a Gaussian curve for the white line on top of an arctangent curve representing the absorption edge. Just as for the XANES edge shift, chemical shift rules also apply to the white line. Because of screening effects caused by the change in electron density, the center of the white line is expected to shift to higher energy with increasing effective oxidation state of the Pt atom. While these indications are strong, corroborations by other techniques that are more sensitive to changes in electronic structure would provide further insight into differences in catalytic reactivity.

2.2. Surface Species in Pt-CTF and Pt(bpym)Cl_2. Platinum interactions with pyridinic surface species of the CTF support were established by XPS analyses of the N 1s core-level electrons (Figure 3). Coordinative modification of CTF or the molecular 2,2′-bipyrimidine ligand with Pt(II) significantly changes the electron density at the pyridinic N sites and thus the binding energies of their N 1s electrons. For unmodified 2,2′-bipyrimidine, a single peak at a binding energy of 398.1 eV is observed, indicating the exclusive presence of pyridinic nitrogen species (Figure 3a). In contrast, two peaks at 398.0 and 399.1 eV are observed for Pt(bpym)Cl_2, indicating the presence of two nitrogen species with almost-identical intensities (Figure 3b). The shift to higher binding energies is a consequence of interactions between the valence electrons of the coordinating N atoms with platinum, and thus, an indication for interactions with pyridinic nitrogen moieties.

For the CTF, a more complicated behavior is observed, associated with the disordered polymer structure (Figure 3d). Deconvolution of the XPS N 1s spectra indicates the presence of three different nitrogen species with different binding energies: pyridine (N-1, 398.1 eV), pyrrole/pyridone (N-2, 399.7 eV), and quaternary (N-3, 401.0 eV) nitrogen species.[30,31] At the high polymerization temperature used (600 °C), some carbonization also occurs, leading to the formation of additional nitrogen species with higher binding energies, in contrast to the exclusive presence of pyridinic nitrogen moieties in the idealized structure. This behavior is commonly observed and well-known for thermally treated nitrogen-containing carbons.[31] As EXAFS also suggests the presence of bidentate N-coordination sites in CTF, it can be considered to be intermediate between polymer and carbonized networks that possess the combined chemical properties/structures of both types of materials.

Analog to Pt(bpym)Cl_2, modification of CTF with Pt^{II} results in a change of the N 1s spectra, i.e., a significant increase of intensity at a binding energy of 399.3 eV (red arrow; Figure 3e), which can also be observed from the raw data (black). These features indicate an interaction of Pt with the pyridinic sites of CTF, similar to its molecular counterpart Pt(bpym)Cl_2. Moreover, measured binding energies of the Pt 4f core level give clear evidence of the exclusive presence of Pt^{II} species within the CTF material (Figure 3c). Comparison of XPS Pt 4f spectra for Pt-CTF materials before and after exposure to reaction conditions provides valuable information about changes in the environment of the active Pt species (Figure 3c). It can be observed that the Pt atoms remain in the same oxidation state as that observed before reaction, although a slight shift in the peak position is noted. In detail, the Pt $4f_{7/2}$ peak after reaction is shifted by 0.5 eV to higher binding energies, which is consistent with the observed white-line shift in XANES spectra. Moreover, minor changes in CTF properties can be observed for Pt-CTF after catalysis in the XPS N 1s spectra (Figure 3f). In comparison to Pt-CTF before exposure to reaction conditions, slight increases in the population of the N-2 and N-3 species are detected, indicating the presence of a higher fraction of nitrogen species with less electron density. This behavior is attributed to electron-withdrawing surface modifications, promoted by oxidation and/or protonation via sulfuric acid under the harsh reaction conditions.

2.3. Distribution of Pt Atoms within Pt-CTF. In addition to the molecular level insights regarding the local Pt environments, their distributions within the Pt-CTF catalyst are important, especially with respect to their stabilities under harsh reaction conditions. Such information can be effectively established by using aberration-corrected high-angle annular dark-field scanning transmission electron microscopy (AC-HAADF-STEM), combined with energy-dispersive X-ray spectroscopy (EDX). Cross-sectional EDX analysis of a Pt-CTF particle reveals a homogeneous distribution of Pt across the particle (Figure 4a). The as-synthesized Pt-CTF material was found to be loaded with 15 wt % Pt, atomically dispersed within the CTF, which is highly unusual for a catalyst with such a high noble-metal content (see Figures 4b and 4c, as well as Figures S5a–c in the Supporting Information). Moreover, Pt sites remain atomically dispersed after several catalytic runs under the harsh conditions of the selective oxidation of methane (i.e., 4 times, 2.5 h, 215 °C, 90 bar CH_4, 20 wt % SO_3). AC-HAADF-STEM images (see Figures 4d and 4e, as well as Figure S6 in the Supporting Information) clearly demonstrate that the material maintains homogeneous distribution of atomic Pt within the CTF, complementing the previously discussed techniques. Overall, Pt-CTF is established to maintain a high degree of atomic Pt dispersion throughout the material before and after the partial oxidation of methane, similar to the molecular catalyst.

3. CONCLUSIONS

The combination of both novel synthesis and novel characterization strategies has yielded unprecedented new insights regarding the molecular level compositions, structures, and properties of a heterogenized molecular Pt catalyst, and its similarities and differences, with respect to its molecular analogue. Specifically, distinct types of Pt sites have been identified within a platinum-functionalized covalent triazine framework (Pt-CTF) that mimics the Periana catalyst in the selective oxidation of methane to methanol. The use of solid-state ^{195}Pt WURST-CPMG NMR has enabled, for the first time, the local coordination environments of ^{195}Pt sites in the Pt-CTF catalyst to be directly measured and quantitatively analyzed. The findings were corroborated by EXAFS, XANES, and XPS structural and surface characterization methods, all of which provided evidence for Pt^{II} coordination to pyridinic nitrogen sites in the Pt-CTF complex, most of which are very similar to one of the two coordination environments in crystalline Pt(bpym)Cl_2. Comparison of results obtained for the Pt-CTF materials before and after their use in the selective oxidation of methane under harsh reaction conditions establishes the overall robustness of the catalyst, accompanied by minor molecular-level changes that are similar to those

DOI: 10.1021/acscatal.5b02305
ACS Catal. 2016, 6, 2332–2340

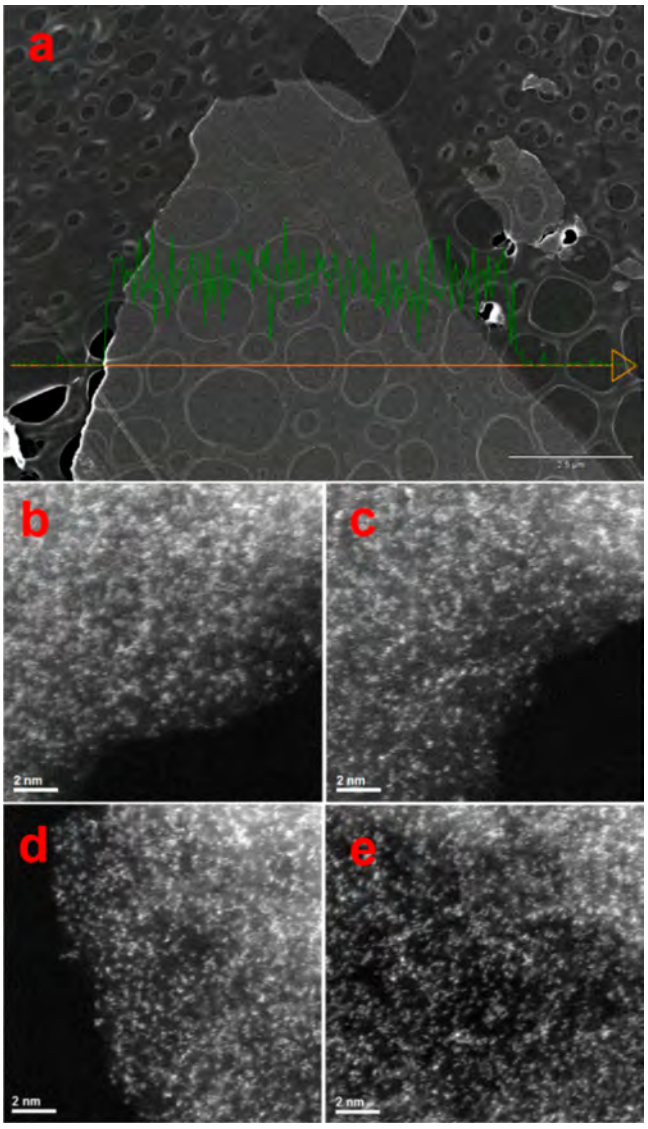

Figure 4. Electron microscopy images of 15 wt % Pt-CTF: (a) EDX line scan of a catalyst cross section; (b–e) AC-HAADF-STEM images of catalysts before (as-made) exposure to reaction conditions (panels (b) and (c)) and after exposure to reaction conditions (4 times, 2.5 h, 215 °C, oleum (20 wt % SO_3), 90 bar CH_4) (panels (d) and (e)), depicting atomic dispersion of Pt in both cases.

suggested for Pt(bpym)Cl_2. These results provide detailed insights on the underlying molecular compositions, structures, and distributions of a heterogenized Periana catalyst and open new opportunities for improving and optimizing its reaction properties. Furthermore, the synthesis and characterization protocols are expected to be generally applicable to other types of heterogeneous Pt catalysts and to other coordinated-metal-complex catalysts more broadly, for which new understanding may be obtained concerning their properties and on the reactions that they promote.

■ ASSOCIATED CONTENT

Supporting Information

The Supporting Information is available free of charge on the ACS Publications website at DOI: 10.1021/acscatal.5b02305.

Characterization details, synthesis procedure for Pt-(bpym)Cl_2 and Pt-CTF, N_2 isotherm of CTF, XRD of CTF and Pt-CTF, thermogravimetry profile of CTF, XPS Pt 4f spectra of Pt-CTF and Pt(bpym)Cl_2, FT-IR of CTF, solid state ^{195}Pt-NMR of Pt(bpym)Cl_2, chemical shift parameters of Pt-CTF and Pt(bpym)Cl_2, solid-state ^{13}C NMR of Pt-CTF, cross-sectional SEM-EDX analysis of Pt-CTF, high-resolution STEM images of CTF and Pt-CTF, XAS spectra and Fourier transforms of Pt-CTF, statistical data of fitted EXAFS functions of Pt-CTF, geometric parameters of EXAFS functions, platinum content of Pt-CTF before and after catalysis and platinum content in five recycling experiments (PDF)

■ AUTHOR INFORMATION

Corresponding Authors

*E-mail: bradc@engineering.ucsb.edu.

*E-mail: schueth@mpi-muelheim.mpg.de.

Present Addresses

[▽]hte GmbH, Heidelberg, D-69123, Germany.

[○]Fraunhofer Institute for Solar Energy Systems, Heidenhofstrasse 2, D-79110 Freiburg, Germany.

[◆]Queen Mary University of London, School of Engineering and Materials Science, Mile End Road, London, U.K.

Author Contributions

[¶]These authors contributed equally. The manuscript was written through contributions of all authors. All authors have given approval to the final version of the manuscript.

Notes

The authors declare no competing financial interest.

■ ACKNOWLEDGMENTS

The solid-state ^{195}Pt NMR measurements were supported by the U.S. National Science Foundation, under Grant No. MSN-CHE-1059108, and were conducted using the Central Facilities of the UCSB Materials Research Laboratory, which was supported by the MRSEC Program of the National Science Foundation (under Award No. DMR-1121053). L.C.J. thanks the NSF-IOSE-PIRE Program (No. 0968399) and the NSF ConvEne IGERT Program (No. NSF-DGE 0801627) for fellowship support. XAS characterization was carried out at beamline C, HASYLAB at DESY, Hamburg. The authors are grateful for Dr. E. Welter for support. TEM work was performed through a user project supported by ORNL's Center for Nanophase Materials Sciences (CNMS), which is a DOE Office of Science User Facility. Financial support by the "ENERCHEM" project house of the Max Planck Society is gratefully acknowledged. Part of this cooperation was initiated within the framework of a Max Planck Society–UCSB research partnership. R.P. acknowledges financial support from the DFG (PA1689/1-1) and Aachen-California Network of Academic Exchange (ACalNet) supported by the DAAD and financed by the German Federal Ministry of Education and Research. T.Z. is grateful for a Kekulé scholarship of the Fonds der Chemischen Industrie.

■ REFERENCES

(1) Thomas, J. M.; Raja, R.; Lewis, D. W. *Angew. Chem., Int. Ed.* **2005**, *44*, 6456–6482.

(2) Anwander, R. In *Handbook of Heterogeneous Catalysis*, 2nd Edition; Ertl, G., Knözinger, H., Schüth, F., Weitkamp, J., Eds.; Wiley–VCH Verlag GmbH & Co. KGaA: Weinheim, Germany, 2008; Vol. 2, p 583.

DOI: 10.1021/acscatal.5b02305
ACS Catal. 2016, 6, 2332–2340

(3) Copéret, C.; Chabanas, M.; Petroff Saint-Arroman, R.; Basset, J.-M. *Angew. Chem., Int. Ed.* **2003**, *42*, 156−181.
(4) Thomas, J. M.; Raja, R.; Gai, P. L.; Grönbeck, H.; Hernández-Garrido, J. C. *ChemCatChem* **2010**, *2*, 402−406.
(5) Thomas, J. M. *Microporous Mesoporous Mater.* **2011**, *146*, 3−10.
(6) Thomas, J. M.; Raja, R. *J. Organomet. Chem.* **2004**, *689*, 4110−4124.
(7) Maschmeyer, T.; Rey, F.; Sankar, G.; Thomas, J. M. *Nature* **1995**, *378*, 159−162.
(8) Jarupatrakorn, J.; Tilley, T. D. *J. Am. Chem. Soc.* **2002**, *124*, 8380−8388.
(9) Corma, A. *Catal. Rev.: Sci. Eng.* **2004**, *46*, 369−417.
(10) Thomas, J. M.; Raja, R. *Catal. Today* **2006**, *117*, 22−31.
(11) Corma, A.; Garcia, H. *Top. Catal.* **2008**, *48*, 8−31.
(12) McNamara, C. A.; Dixon, M. J.; Bradley, M. *Chem. Rev.* **2002**, *102*, 3275−3300.
(13) Periana, R. A.; Taube, D. J.; Gamble, S.; Taube, H.; Satoh, T.; Fujii, H. *Science* **1998**, *280*, 560−564.
(14) Conley, B. L.; Tenn, W. J.; Young, K. J. H.; Ganesh, S.; Meier, S.; Ziatdinov, V.; Mironov, O.; Oxgaard, J.; Gonzales, J.; Goddard, W. A.; Periana, R. A. In *Activation of Small Molecules: Organometallic and Bioinorganic Perspectives*, 1st Edition; Tolman, W. B., Ed.; Wiley−VCH Verlag GmbH & Co. KGaA: Weinheim, Germany, 2006; Chapter 7, p 254.
(15) Kuhn, P.; Antonietti, M.; Thomas, A. *Angew. Chem., Int. Ed.* **2008**, *47*, 3450−3453.
(16) Kuhn, P.; Thomas, A.; Antonietti, M. *Macromolecules* **2009**, *42*, 319−326.
(17) Palkovits, R.; Antonietti, M.; Kuhn, P.; Thomas, A.; Schüth, F. *Angew. Chem., Int. Ed.* **2009**, *48*, 6909−6912.
(18) Soorholtz, M.; White, R. J.; Zimmermann, T.; Titirici, M.-M.; Antonietti, M.; Palkovits, R.; Schuth, F. *Chem. Commun.* **2013**, *49*, 240−242.
(19) O'Dell, L. A.; Schurko, R. W. *Chem. Phys. Lett.* **2008**, *464*, 97−102.
(20) MacGregor, A. W.; O'Dell, L. A.; Schurko, R. W. *J. Magn. Reson.* **2011**, *208*, 103−113.
(21) Lucier, B. E. G.; Reidel, A. R.; Schurko, R. W. *Can. J. Chem.* **2011**, *89*, 919−937.
(22) Still, B. M.; Kumar, P. G. A.; Aldrich-Wright, J. R.; Price, W. S. *Chem. Soc. Rev.* **2007**, *36*, 665−686.
(23) Widdifield, C. M.; Schurko, R. W. *Concepts Magn. Reson., Part A* **2009**, *34A*, 91−123.
(24) Kaim, W.; Dogan, A.; Wanner, M.; Klein, A.; Tiritiris, I.; Schleid, T.; Stufkens, D. J.; Snoeck, T. L.; McInnes, E. J. L.; Fiedler, J.; Záliš, S. *Inorg. Chem.* **2002**, *41*, 4139−4148.
(25) Gomes, J. A. N. F.; Mallion, R. B. *Chem. Rev.* **2001**, *101*, 1349−1384.
(26) Mironov, O. A.; Bischof, S. M.; Konnick, M. M.; Hashiguchi, B. G.; Ziatdinov, V. R.; Goddard, W. A., III; Ahlquist, M.; Periana, R. A. *J. Am. Chem. Soc.* **2013**, *135*, 14644−14658.
(27) Xu, X.; Kua, J.; Periana, R. A.; Goddard, W. A. *Organometallics* **2003**, *22*, 2057−2068.
(28) Kua, J.; Xu, X.; Periana, R. A.; Goddard, W. A. *Organometallics* **2002**, *21*, 511−525.
(29) Øien, S.; Agostini, G.; Svelle, S.; Borfecchia, E.; Lomachenko, K. A.; Mino, L.; Gallo, E.; Bordiga, S.; Olsbye, U.; Lillerud, K. P.; Lamberti, C. *Chem. Mater.* **2015**, *27*, 1042−1056.
(30) Weidenthaler, C.; Lu, A.-H.; Schmidt, W.; Schüth, F. *Microporous Mesoporous Mater.* **2006**, *88*, 238−243.
(31) Arrigo, R.; Havecker, M.; Schlögl, R.; Su, D. S. *Chem. Commun.* **2008**, *40*, 4891−4893.

DOI: 10.1021/acscatal.5b02305
ACS Catal. 2016, 6, 2332−2340

Supporting Information

Local platinum environments in a solid analog of the molecular Periana catalyst

Mario Soorholtz,[a,†,‡] Louis C. Jones,[b,†] Dominik Samuelis,[c] Claudia Weidenthaler,[a] Robin J. White,[d,#] Maria-Magdalena Titirici,[d] David A. Cullen,[e] Tobias Zimmermann,[a] Markus Antonietti,[d] Joachim Maier,[c] Regina Palkovits,[a,f] Bradley F. Chmelka,[b,*] and Ferdi Schüth[a,*]

[a] Max-Plank-Institut für Kohlenforschung, Mülheim an der Ruhr, D-45470, Germany
[b] Department of Chemical Engineering, University of California, Santa Barbara, California 93106-5080, USA
[c] Max Planck Institute for Solid State Research, Stuttgart, D-70569, Germany
[d] Max Planck Institute of Colloids and Interfaces, Potsdam, D-14476, Germany
[e] Oak Ridge National Laboratory, Oak Ridge, Tennessee 37831, USA
[f] RWTH Aachen University, Aachen, D-52074, Germany

Corresponding Author

* bradc@engineering.ucsb.edu

* schueth@mpi-muelheim.mpg.de

Table of Content:

Characterization Details

X-ray absorption spectroscopy (XAS) at the platinum L_3 edge (E_0=11564 eV) was performed at HASYLAB@DESY beamline C. Spectra were recorded *ex situ* in a LN_2 cryostat at 77K in transmission geometry, using ion chambers as detectors (first ion chamber: 150 mbar Kr; second and third ion chamber: 900 mbar Kr). Energy range was [11364;12164] eV, with ΔE=10 eV steps in the pre-edge range to 11534 eV, ΔE=1 eV steps up to 11554 eV, ΔE=0.5 eV steps to 11574 eV (covering the edge step), ΔE=1 eV steps to 11574 eV, and finally *k*-space equidistant scanning with Δk=0.025 between 11574 and 12164 eV. Sampling time was 1 second for each data point in constant-ΔE scanning and from 1 to 4 seconds for constant-Δk scanning. A platinum foil reference for energy calibration, placed between second and third ion chamber, was measured simultaneously. In order to avoid higher harmonics passing the Si(111) double crystal monochromator, the second crystal was detuned to 50% of the maximum intensity, using the D-Mostab monochromator stabilization system.[1, 2] Sample pellets for transmission measurements were prepared by homogenizing between 15 and 30 mg of the finely ground catalyst sample with approx. 40 mg binder/diluent, consisting of (80:20) cellulose (Aldrich) and graphite powder (Aldrich) for improved heat conduction, followed by uniaxial pressing at 30 kN for 60 s, and yielding a self-supporting pellet with d=12 mm. Three to four spectra were recorded per sample. After checking for reproducibility, spectra were aligned in E-space and energy-calibrated *via* the Pt reference foil spectra. EXAFS spectra were extracted from the merged data according to the standard procedures, using the IFEFFIT/HORAE[3, 4] software suite and the AutoBK[5] algorithm. The geometrical model for the EXAFS refinement was based on coordinates of the

analogous homogeneous catalyst Pt(bpym)Cl_2, obtained from DFT-based geometry optimization.

High resolution high-angle annular dark-field (HAADF) STEM images were recorded using a JEOL 2200FS operated at 200 kV and equipped with a CEOS GmbH hexapole aberration corrector, which provides a sub-Angstrom electron probe for imaging and spectroscopic analysis. Powders were sonicated in methanol and then evaporatively dispersed on the TEM grids.

Solid-state ^{195}Pt WURST-CPMG NMR spectra were acquired at 7.06 T on a Bruker AVANCE NMR spectrometer operating at 300.07 and 64.49 MHz for ^{1}H and ^{195}Pt, respectively, with parameters optimized according to references.[6, 7] WURST-CPMG pulses of 50 μs (~2 MHz) were applied at center frequencies of 64.72 and 64.28 MHz using forward and reverse frequency sweeps to compensate for transverse relaxation of ^{195}Pt magnetization during the sweeps. An acquisition time of 80 μs was used to measure the free induction decays of each subsequent CPMG loop (12 total) with recycle delays of 0.5 to 2 s, which were chosen to maximize signal sensitivity. Fourier transformed spectra for the two center frequencies were co-added after a magnitude calculation to produce the observed ^{195}Pt spikelet patterns with a span of >1 MHz. Lineshape analyses were performed using the program *dmfit* based on interpolated skyline projections of each characteristic CPMG spikelet pattern.[8] ^{195}Pt chemical shifts are referenced with respect to 1.0 M Na_2PtCl_6 (aq) (δ_{iso}=0.0 ppm).

Nitrogen sorption measurement was carried out at 77 K on a Micrometrics ASAP 2010 instrument. Samples were activated under vacuum for at least 15 h at 150 °C. Pore size distribution, pore volume and surface area were calculated using Autosorb software

(version 1.52) using the NLDFT equilibrium model (N_2 at 77K on carbon (slit/cylindrical pore model). Comparison of calculated NLDFT and measured sorption data exhibit a match of > 97%.

XRD patterns were collected with a Bragg Brentano diffractometer (STOE THETA/THETA). The instrument was equipped with a secondary graphite monochromator (Cu$K_{\alpha 1,2}$ radiation) and a proportional gas detector. The divergence slit was set to 0.8°, the receiving slit was set to 0.8 mm, and the width of the horizontal mask was 4 mm. The samples were prepared on a background free single crystal quartz sample holder.

Thermogravimetry experiments were performed using a Netzsch STA 449C thermal analyzer applying a heating rate of 10°C min^{-1} in a flow of air (60 mL min^{-1}).

FT-IR spectra were recorded on a Magna System 560 equipped with a Ge-ATR-crystal. Each sample was scanned 128 times with a resolution of 2 cm^{-1}.

XPS (X-ray photoelectron spectroscopy) measurements were performed with a Kratos HSi spectrometer with a hemispherical analyzer. The monochromatized Al K_α X-ray source (E=1486.6 eV) was operated at 15 kV and 15 mA. For the narrow scans, an analyzer pass energy of 40 eV was applied. The hybrid mode was used as lens mode. The base pressure during the experiment in the analysis chamber was 4 x 10^{-7} Pa. To consider surface charging effects of carbonized samples, the binding energy values were referenced to the graphitic C 1s carbon peak at 284.5 eV. CTF materials were measured as pressed pellets with a fraction of (nitrogen free) cellulose (mass ratio: CTF/cellulose = ~3) in order to fix the sample within the XPS chamber. Accuracy of given binding energies is in the range of ±0.2 eV.

Scanning electron microscopy (SEM) micrographs were collected on a Hitachi S-5500 ultra-high resolution cold field emission scanning electron microscope. The instrument was operated at a maximum acceleration voltage of 30 kV.The samples were embedded in Spurr resin (hard-mixture) in a two-step procedure. After trimming the tip to around 150μm², a Diamond-knife in an Ultramicrotom (Reichert Ultracut) was used for sectioning. The thickness of the sections is around 30 nm.

The ^{13}C CP-MAS NMR spectrum was recorded on a Bruker Avance 500WB spectrometer at a resonance frequency of 125.8 MHz using a double-bearing MAS probe (DVT BL4). The experimental conditions were as follows: 12 kHz spinning rate, 2 s recycle delay, 27,300 scans, 1 ms contact time, and 4.3 μs ^{1}H $\pi/2$ pulse. The chemical shift was referenced to neat TMS in a separate rotor.

TEM micrographs of Figure S9 were obtained on an HF-2000 instrument. The HF-2000 instrument is equipped with a cold field emitter (CFE) and can be operated at a maximum acceleration voltage of 200 kV. Typically the samples were placed on a Lacey carbon film supported by a copper grid. Solid samples were deposited on the Lacey carbon film without previous dissolution.

Experimental Details

Covalent Triazine Framework (CTF) was synthesized according to the method of Kuhn *et al.*[9]. Zinc chloride and 2,6-dicyanopyridine were stored in a glove box after intensive drying in high vacuum (10^{-3} mbar) at 150°C for 30°C, respectively. 3.362 g (0.025 mol) $ZnCl_2$ and 0.646 g (0.005 mol) 2,6-dicyanopyridine were thoroughly mixed and filled into a quartz ampule (12 x 1 cm). This ampule was evacuated, sealed and placed into an ampule oven with no temperature gradients. The sample was thermally treated at 400°C with a heating rate of 15°C min^{-1} and a hold time of 40 h in a first sequence. In a second sequence, the sample was treated at 600°C with a heating ramp of 10°C min^{-1} and a hold time of 40 h before the sample was cooled down to room temperature. After opening the quartz ampule, the monolithic material was intensively washed with water and hydrochloric acid. Finally, the sample was dried in a vacuum oven at 50°C.

Dichlorobipyrimidyl platinum(II) ($Pt(bpym)Cl_2$) was synthesized as described according to the method of Kiernan *et al*[10]. For the coordination of platinum to the solid material, analogous to the method of P. M. Kiernan *et al.*[10] and Ziatdinov[11], 400 mg of the carbon was added to 1 L water that contained 46 mg of dissolved K_2PtCl_4. The mixture was stirred for 24 h at room temperature. After filtration, the solid was intensively washed with water to remove non-coordinated Pt species.

References

(1) Krolzig, A.; Materlik, G.; Swars, M.; Zegenhagen, J. *Nucl. Instr.Meth. Phys. Res.* **1984**, *219*, 430-434.

(2) Meß, K.; Tröger, L.; Brüggemann, U. In *HASYLAB Annual Report 1998*, Laasch, W., Materlik, G., Schneider, J. R., Schulte-Schrepping, H., Eds.; Hamburger Synchrotonstrahlungslabor HASYLAB, Hamburg, Germany, 1998.

(3) Ravel, B.; Newville, M. *J. Synchrotron Radiat.* **2005**, *12*, 537-541.

(4) Newville, M. *J. Synchrotron Radiat.* **2001**, *8*, 322-324.

(5) Newville, M.; Līviņš, P.; Yacoby, Y.; Rehr, J. J.; Stern, E. A. *Phys. Rev. B* **1993**, *47*, 14126-14131.

(6) O'Dell, L. A.; Schurko, R. W. *Chem. Phys. Lett.* **2008**, *464*, 97-102.

(7) MacGregor, A. W.; O'Dell, L. A.; Schurko, R. W. *J. Magn. Reson.* **2011**, *208*, 103-113.

(8) Massiot, D.; Fayon, F.; Capron, M.; King, I.; Le Calvé, S.; Alonso, B.; Durand, J.-O.; Bujoli, B.; Gan, Z.; Hoatson, G. *Magn. Reson. Chem.* **2002**, *40*, 70-76.

(9) Kuhn, P.; Thomas, A.; Antonietti, M. *Macromolecules* **2009**, *42*, 319-326.

(10) Kiernan, P. M.; Ludi, A. *Dalton Trans.* **1978**, 1127-1130.

(11) Ziatdinov, V. R. Dissertation, University of Southern California, 2007.

(12) Xu, X.; Kua, J.; Periana, R. A.; Goddard, W. A. *Organometallics* **2003**, *22*, 2057-2068.

Supplementary Results

X-ray diffraction (XRD):

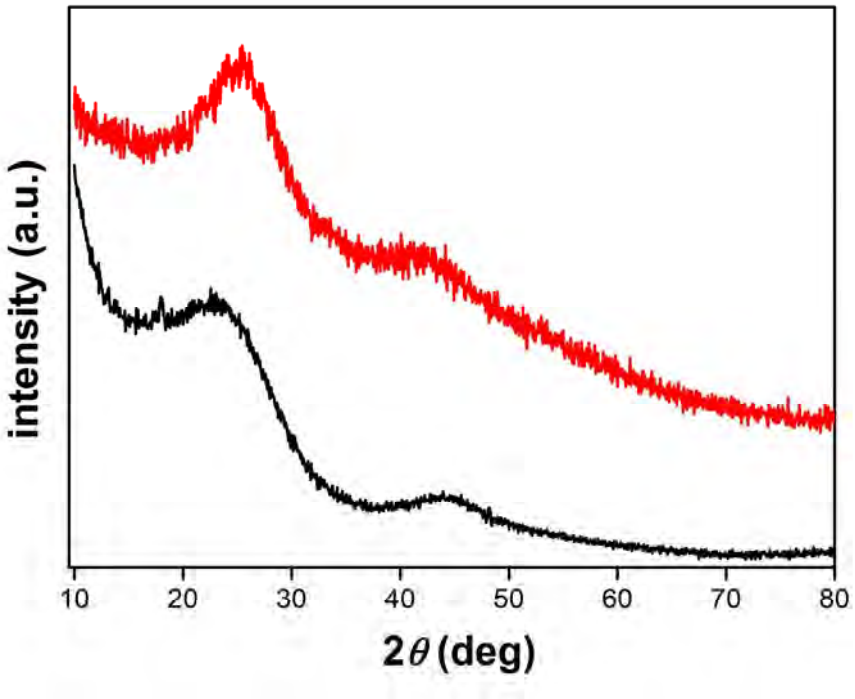

Figure S1. Powder XRD patterns of non-modified CTF (black) and Pt-modified CTF (red). Both XRD patterns exhibit characteristics for carbon materials with aromatic stacking. Moreover, no reflections for metallic platinum can be observed for Pt-modified CTF. Minor differences in lineshape can be attributed to different particle sizes between CTF and Pt-CTF.

Solid-State ^{195}Pt NMR

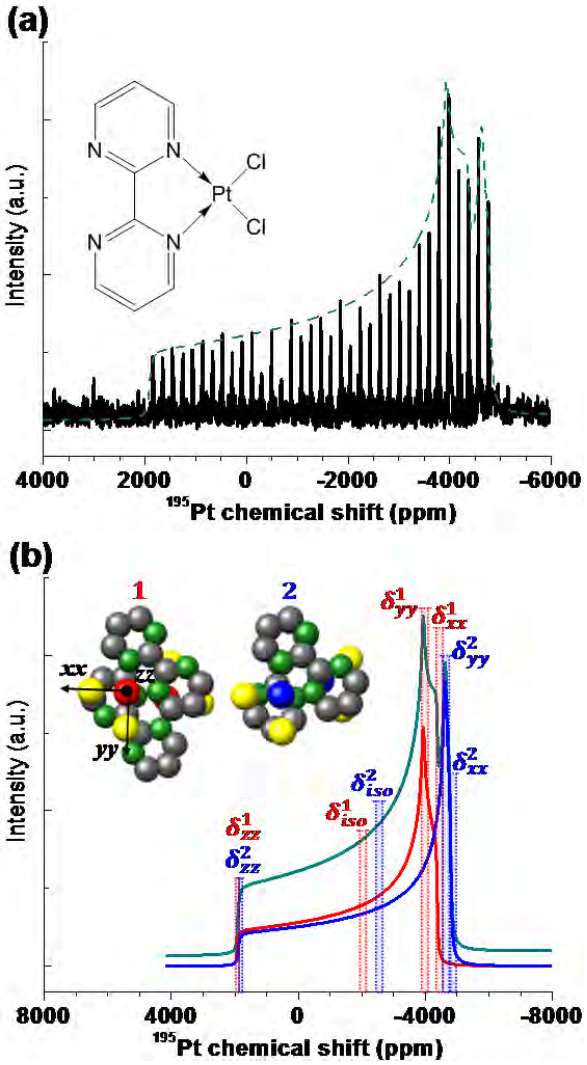

Figure S2. (a) Static solid-state ^{195}Pt WURST-CPMG NMR spectrum (black) and summed fit (dashed green) of **(b)** lineshapes that correspond to the two distinct equally populated ^{195}Pt atom sites in crystalline (bpym)$PtCl_2$. Proposed local structures of the ^{195}Pt sites (1, red; 2, blue) are shown as insets above each spectrum, with nitrogen atoms (green), carbon atoms (grey), and chlorine atoms (yellow). Chemical shift parameters (δ_{xx}, δ_{yy}, δ_{zz}, and δ_{iso}) are descriptors of the local ^{195}Pt bonding environments and are indicated for each lineshape, specific values of which are tabulated in Table S3. Axes shown for site 1 indicate the orthogonal coordinate system of the site's ^{195}Pt chemical shift tensor.

Table S1. ^{195}Pt chemical shift parameters for as-synthesized Pt-CTF catalyst

Chemical Shift Tensor Parameters [ppm]				Chemical Shift Anisotropy Parameters			
Component	δ_{xx}	δ_{yy}	δ_{zz}	δ_{iso} [ppm]	$\Delta\sigma/\Delta\delta$ [ppm]	η	% Area
I	-4900 +/- 200	-4500 +/- 200	6400 +/- 200	-1000 +/- 200	7400 +/- 400	0.06 +/- 0.04	75 +/- 10
II	NA	NA	NA	-4200 +/- 200	1500 +/- 400	NA	25 +/- 10

Table S2. ^{195}Pt chemical shift parameters for used Pt-CTF catalyst after reaction.

Chemical Shift Tensor Parameters [ppm]				Chemical Shift Anisotropy Parameters			
Component	δ_{xx}	δ_{yy}	δ_{zz}	δ_{iso} [ppm]	$\Delta\sigma/\Delta\delta$ [ppm]	η	% Area
I	-4900 +/- 200	-4500 +/- 200	6400 +/- 4500	-1000 +/- 1500	7400 +/- 400	0.06 +/- 0.04	53 +/- 10
II	NA	NA	NA	-4200 +/- 200	1500 +/- 400	NA	47 +/- 10

Table S3. ^{195}Pt chemical shift parameters for polycrystalline Pt(bpym)Cl_2.

Chemical Shift Tensor Parameters [ppm]				Chemical Shift Anisotropy Parameters			
Component	δ_{xx}	δ_{yy}	δ_{zz}	δ_{iso} [ppm]	$\Delta\sigma$ [ppm]	η	% Area
1	-4400 +/- 200	-3900 +/- 200	1900 +/- 200	-2100 +/- 200	4100 +/- 400	0.11 +/- 0.04	50 +/- 5
2	-4800 +/- 200	-4600 +/- 200	1900 +/- 200	-2500 +/- 200	4400 +/- 400	0.04 +/- 0.04	50 +/- 5

Catalyst recycling

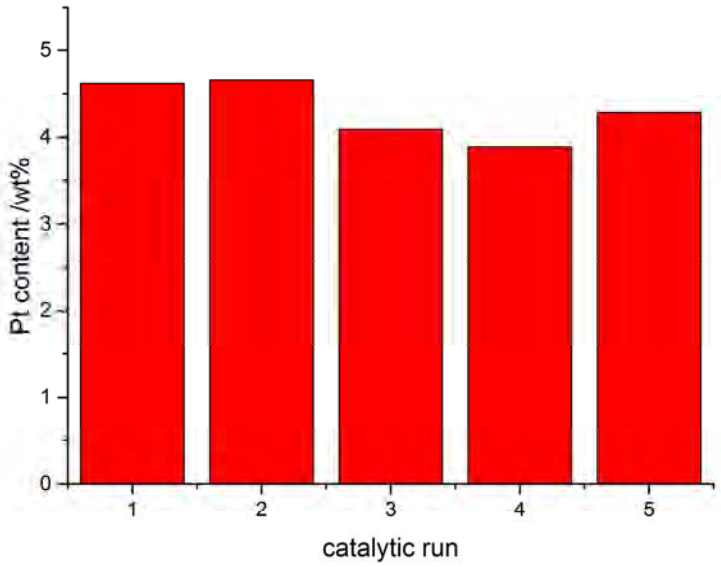

Figure S3. Platinum content of Pt-CTF in recycling experiments. Pt-CTF (~5 wt% Pt) was tested in 5 subsequent catalytic runs (reaction conditions: 215°C, 2.5 h, 15 mL oleum (20 wt.% SO_3), 90 bar CH_4) and analyzed for its platinum content. After each run the catalyst was filtered off at room temperature from the reaction solution and thoroughly washed with water and acetone. After drying an aliquot was analyzed for its platinum content (atomic absorption spectroscopy, AAS, Mikroanalytisches Laboratorium Kolbe, Mülheim) and the residual catalyst used in the next experimental run. These experiments indicate a stable platinum loading of ~4-5 wt% for the Pt-CTF material used under these conditions over five subsequent experiments.

Table S4. Platinum contents of Pt-CTFs before and after catalysis measured with various techniques.

measurement	*platinum content before /wt%*	*platinum content after /wt%*
AAS	15.0	6.7
XAS	27.5 ±13.3	4.1 ±2.0
XPS	18.2	n.a.
SEM-EDX	15.0	n.a.

Samples before catalysis were measured with high metal contents in favor of a high S/N ratio. Samples after catalysis showed a lower S/N ratio consistent with partial leaching of platinum.

X-Ray Absorption Spectroscopy (XAS)

Table S5. Mass fraction of platinum within Pt-CTF samples. Metal concentrations were determined by dividing the edge step Δμ by catalyst mass present in pellets (assuming homogeneous distribution of platinum throughout the sample pellet, identical diameter of all pellets, and constant X-ray beam size). High error limits were obtained due to the low transition metal content of investigated sample pellets and, thus, due to high signal/noise ratio.

sample	*$mass_{platinum}$ [wt.%]*	*limit of error [wt.%]*
Pt-CTF-(sample 1)	27.5	± 13.3
Pt-CTF-(sample 2)	22.1	± 10.7
Pt-CTF-(sample 3)	17.9	± 8.7
Pt-CTF-(sample 4)	7.9	± 3.8
Pt-CTF-(sample 1)‡	4.1	± 2.0

‡= sample tested under reaction conditions prior to XAS measurement (reaction conditions: 215°C, 2.5 h, 15 mL oleum (20 wt.% SO3), 90 bar CH4).

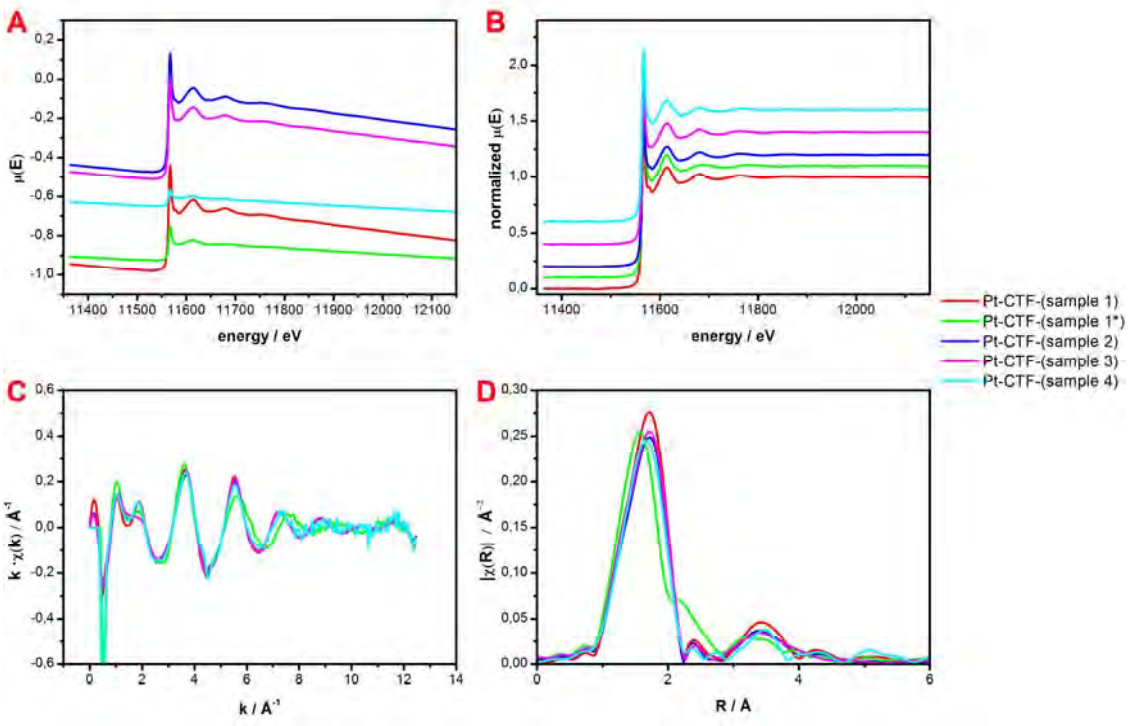

Figure S4. X-ray absorption spectroscopy data. * = sample tested under reaction conditions prior to XAS measurement (reaction conditions: 215°C, 2.5 h, 15 mL oleum (20 wt.% SO_3), 90 bar CH_4); (A) μ(E) raw data; (B) normalized μ(E) data (offsets were introduced in order to visually differentiate samples); (C) χ(*k*)·*k* functions; (D) Fourier-transformed χ(*k*)·*k* functions for investigated Pt-CTF samples. As mentioned above, a first-shell EXAFS fit was complicated by the fact that the expected Pt-N distance (2.05 Å) is similar to the

(non-bonding) Pt-C distance (2.89 Å) for the two carbon atoms bridging the pyrimidine rings, and also from the distance to the next-nearest Pt-C (3.05 Å). In addition, there are two more ligands bound to the Pt, and their distances from the Pt center are approximately 2.4 Å. All of this leads to a very broad first shell signal in the EXAFS spectra; isolation and speciation of the overlapping individual contributions by fitting the EXAFS has to be based on a number of constraints to interpret the information content of the spectra. EXAFS fitting was applied to one Pt-CTF sample that was used in the direct oxidation of methane in sulfuric acid and a series of as-prepared Pt-CTF materials. Fits were done with multiple k-weights, *i.e.* k=1 and k=2 simultaneously. As shown, we were able to fit all pre-catalysis EXAFS spectra with identical structural models, assuming the first coordination shell to contain the (bpym) ligand and 2 Cl^- ligands, and assuming a mirror plane along the Pt – (midpoint C5/C6) axis and perpendicular to the C5/C6 bond (see Fig. 2A), with very high fit quality. Multiple scattering paths had to be included to account for the significant intensity in the region of 3 Å < R_{EXAFS} < 4 Å.

Table S6. Statistical data and amplitude factor S_0^2 of fitted EXAFS functions.

sample	*R factor*	S_0^2	*limit of error for* S_0^2
Pt-CTF-(sample 1)	0.0226	0.8775	± 0.1114
Pt-CTF-(sample 2)	0.0260	0.8350	± 0.1286
Pt-CTF-(sample 3)	0.0193	0.7925	± 0.0882
Pt-CTF-(sample 4)	0.0214	0.8296	± 0.0963
Pt-CTF-(sample 1)*†	0.0369	0.8394	± 0.1317
Pt-CTF-(sample 1)*‡	0.0246	0.9231	± 0.2061

*= sample tested under reaction conditions prior to XAS measurement (reaction conditions: 215°C, 2.5 h, 15 mL oleum (20 wt.% SO3), 90 bar CH4). †Pt(bipym)Cl(HSO_4) model ‡Pt(bpym)Cl_2 model

Table S7a. Geometric parameters of fitted EXAFS functions. Bond descriptions can be taken from Figure 2A. (* = values were derived from structural model taken from Xu *et al.*[12])

sample	*distance Pt-N1 [Å]*	*±[Å]*	*distance Pt-Cl [Å]*	*±[Å]*	*distance Pt-C4 [Å]*	*±[Å]*	*distance Pt-C1 [Å]*	*±[Å]*
$Pt(bpym)Cl_2$*	2.047	0.000	2.375	0.000	2.895	0.000	3.054	0.000
Pt-CTF-(sample 1)	1.965	0.055	2.258	0.046	2.759	0.051	2.912	0.052
Pt-CTF-(sample 2)	1.967	0.053	2.260	0.045	2.763	0.050	2.916	0.052
Pt-CTF-(sample 3)	1.949	0.064	2.248	0.054	2.757	0.059	2.912	0.061
Pt-CTF-(sample 4)	1.965	0.050	2.259	0.043	2.760	0.048	2.913	0.049
Pt-CTF-(sample 1)‡	1.947		2.161		2.656		2.808	

‡ sample used in the selective oxidation of methane; distances are considerable different indicating the invalidity of the $Pt(bpym)Cl_2$ model for this sample

Table S7b. Geometric parameters of fitted EXAFS functions. Bond descriptions can be taken from Figure 2A. (* = values were derived from structural model taken from Xu *et al.* [12])

sample	*distance Pt-N2 [Å]*	*± [Å]*	*distance Pt-C2 [Å]*	*±[Å]*	*distance Pt-C3 [Å]*	*±[Å]*
$Pt(bpym)Cl_2$*	4.183	0.000	4.333	0.000	4.747	0.000
Pt-CTF-(sample 1)	4.027	0.076	4.147	0.065	4.547	0.069
Pt-CTF-(sample 2)	4.033	0.074	4.154	0.065	4.554	0.069
Pt-CTF-(sample 3)	4.043	0.088	4.166	0.076	4.571	0.080
Pt-CTF-(sample 4)	4.027	0.070	4.148	0.061	4.548	0.065
Pt-CTF-(sample 1)‡	3.986		4.029		4.424	

Table S8. Variance σ^2 of various scattering pathways. Bond descriptions can be taken from Figure 2A.

sample	*Pt-N1*	±	*Pt-Cl*	±	*Pt-C1 and Pt-C4*	±	*Pt-N2*	±
$Pt(bpym)Cl_2$	-	-	-	-	-	-	-	-
Pt-CTF-(sample 1)	-0.0007	0.0027	0.0009	0.0019	0.0307	0.0165	-0.0015	0.0065
Pt-CTF-(sample 2)	-0.0006	0.0023	0.0006	0.0016	0.0369	0.0192	-0.0010	0.0059
Pt-CTF-(sample 3)	-0.0004	0.0030	0.0030	0.0026	0.0366	0.0232	3.6885	3566959
Pt-CTF-(sample 4)	-0.0009	0.0022	0.0005	0.0016	0.0354	0.0173	-0.0017	0.0053
Pt-CTF-(sample 1)‡	0.0023	0.0035	0.0086	0.0049	0.0039	0.0072	0.1049	0.4627

‡sample used in the selective oxidation of methane; l

Table S9. First shell coordination numbers for Pt-CTF after use in catalysis. First shell content as refined from EXAFS fits with a model comprising Pt-N, Pt-Cl contributions from the $Pt(bpym)Cl_2$ and Pt-O contributions from OSO_3H ligand. Standard reaction conditions: 2.5h (215°C, 15 mL oleum (20 wt.% SO_3), 90 bar CH_4).

sample	*coordination number for*				
	N	±	*O*	±	*Cl*
Pt-CTF-(sample1)‡	1.94494	0.53540	1.06574	0.3746	0.98932
Pt-CTF-(sample 2)‡	1.48766	0.55540	1.20588	0.48115	1.30640
Pt-CTF-(sample 3)‡	1,80882	0,46070	1,08121	0,35302	1,10997
Pt-CTF-(sample 4)‡	2,06225	0,56203	1,00658	0,33698	0,93116

Electron microscopy

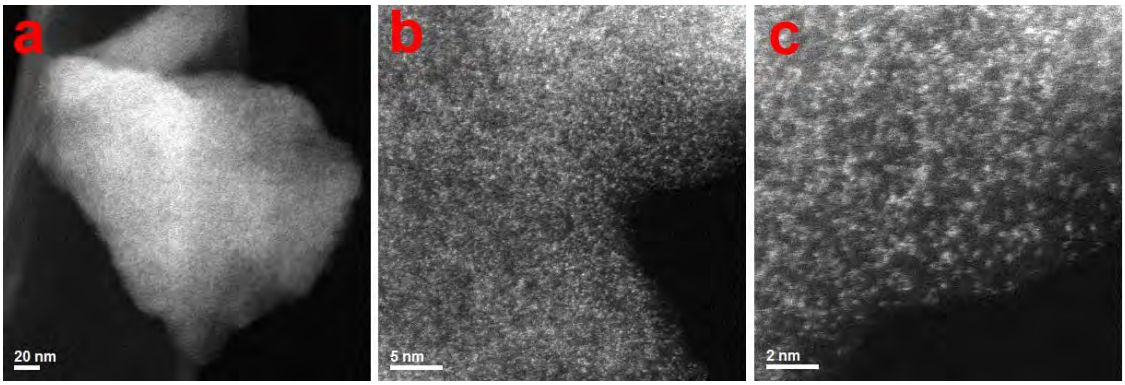

Figure S5. Electron microscopy analysis of Pt-CTF. AC-HAADF-STEM images of Pt-CTF material before use in catalysis clearly show the presence of atomic Pt species. Atomic dispersion was best demonstrated at the thin edges of the CTF particles, where overlap and thickness effects could be avoided.

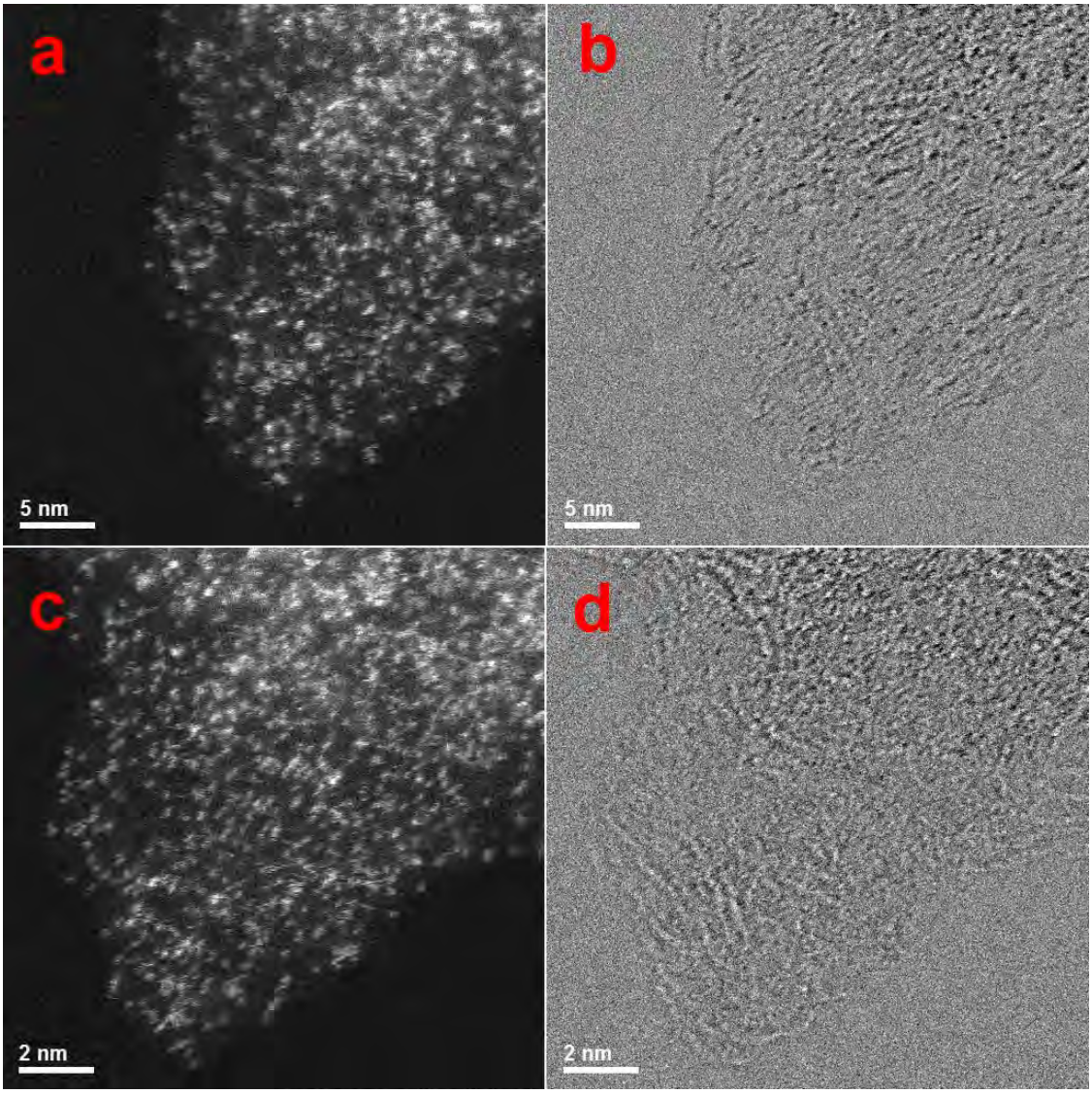

Figure S6. Electron microscopy analysis of Pt-CTF after catalysis. HAADF (**a+c**) and bright-field (**b+d**) STEM images of respective identical locations of Pt-CTF material after several catalytic runs clearly shows that the homogeneous dispersion of single Pt atoms is maintained.

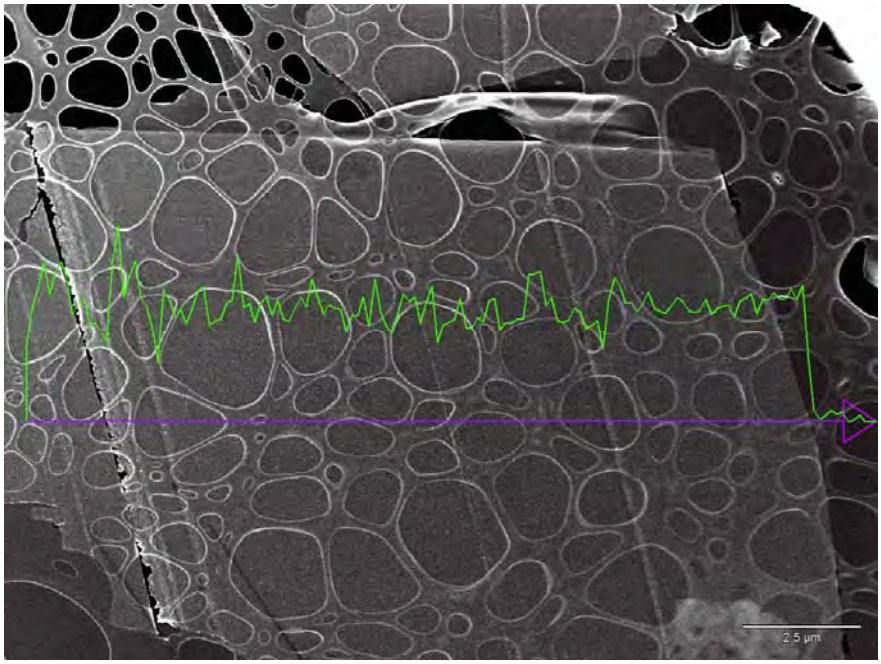

Figure S7. EDX analysis of Pt-CTF. SEM image of a cross-section cut of Pt-CTF with a thickness of around 30 nm. Green line indicates EDX signal referring to Pt, purple arrow demonstrates position of electron beam during analysis.

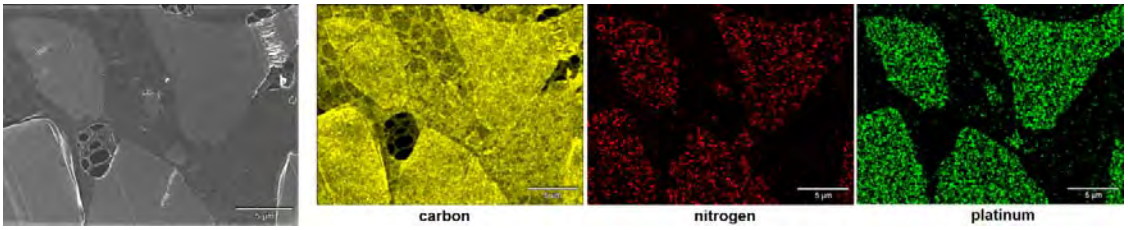

Figure S8. EDX analysis of Pt-CTF. SEM image of Pt-CTF cross-section cuts and the corresponding EDX mapping for carbon, nitrogen and platinum. A homogeneous distribution of Pt within the CTF particles can be observed. In the case of EDX mapping of carbon, species between cuts can be found since Pt-CTF particles are embedded in a carbon-based polymer during sample preparation.

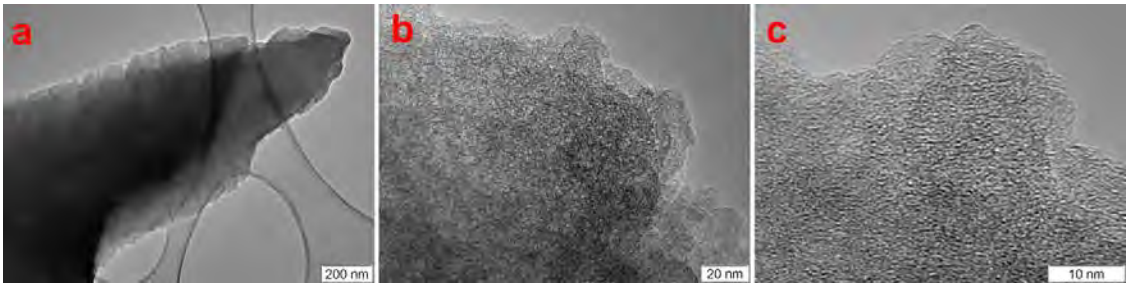

Figure S9. Electron microscopy analysis of CTF. TEM images (**a-c**) illustrate CTF morphology of a representative carbon particle.

Nitrogen sorption

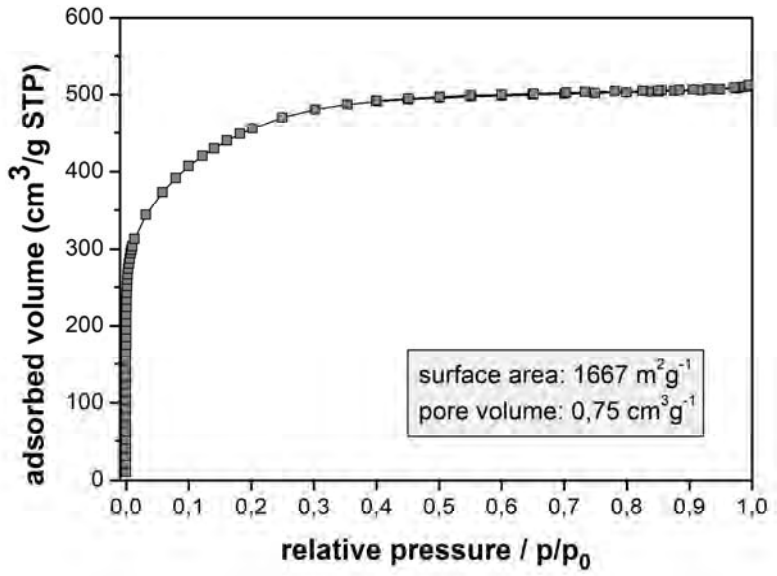

Figure S10. N_2 sorption isotherm of CTF. N_2 sorption for non-modified CTF material based on 2,6-dicyanopyridine as monomer exhibits a Type I-like isotherm. Specific surface area and pore volume of CTF were calculated from NLDFT equilibrium model (see inset).

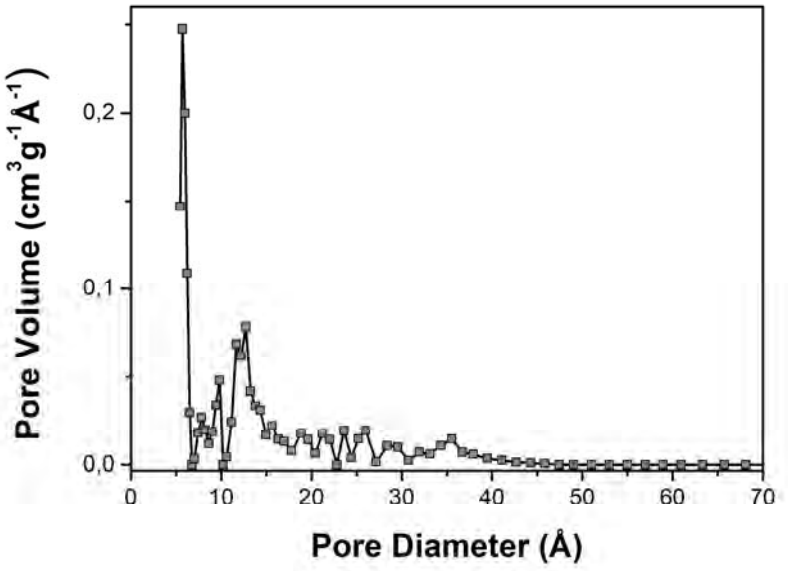

Figure S11. NLDFT pore size distribution for non-modified CTF material. Calculated pore size distribution for CTF material clearly shows its microporous character, however, a relatively small fraction of mesopores with a pore size > 2 nm are present as well.

Thermogravimetry (TG):

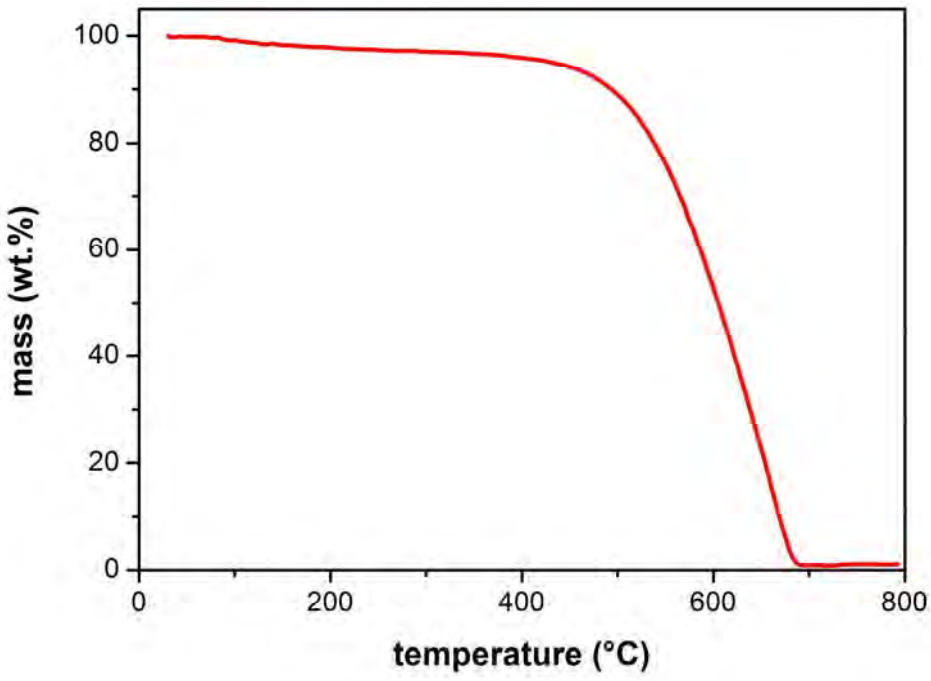

Figure S12. Thermogravimetry profile of CTF in air. Thermogravimetry investigation of CTF material in a flow of air (60 mL min^{-1}) with a heating rate of 10°C min^{-1} indicates good thermal stability of the carbon framework. In detail, significant weight loss can only be observed at temperatures > 400°C, which can be attributed to the oxidation of the carbon scaffold and the formation of CO_2.

X-ray photoelectron spectroscopy (XPS)

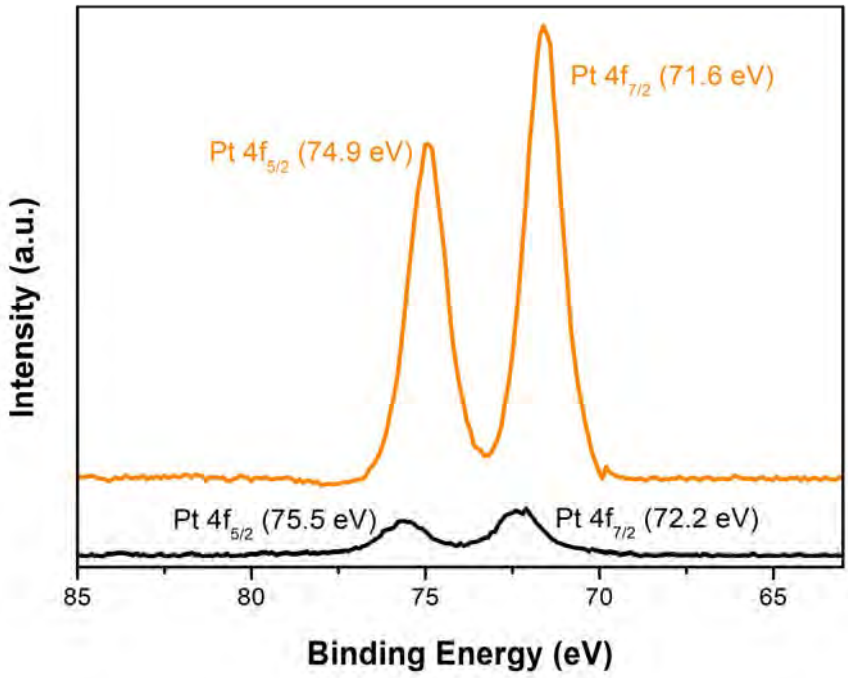

Figure S13. XPS Pt *4f* spectra for Pt-CTF and Pt(bpym)Cl_2. Accurate comparison of Pt 4f binding energies for Pt(bpym)Cl_2 (orange) and Pt-CTF (black) is challenging since determination of a common C 1s reference peak is hardly possible. The graphitic C 1s peak is normally used as reference peak for the investigation of carbon materials (see *Characterization Details*). However, since graphitic carbon is not present in the structure of 2,2'-bipyrimidine and both materials do not share a common defined C 1s peak an accurate comparison is not feasible and, thus, the interpretation of relative peak positions is difficult. Different intensities in Pt 4f spectra are attributed to different weight fractions of platinum in Pt-CTF and Pt(bpym)Cl_2, respectively.

FT-IR Spectroscopy: Attenuated Total Reflectance (ATR)

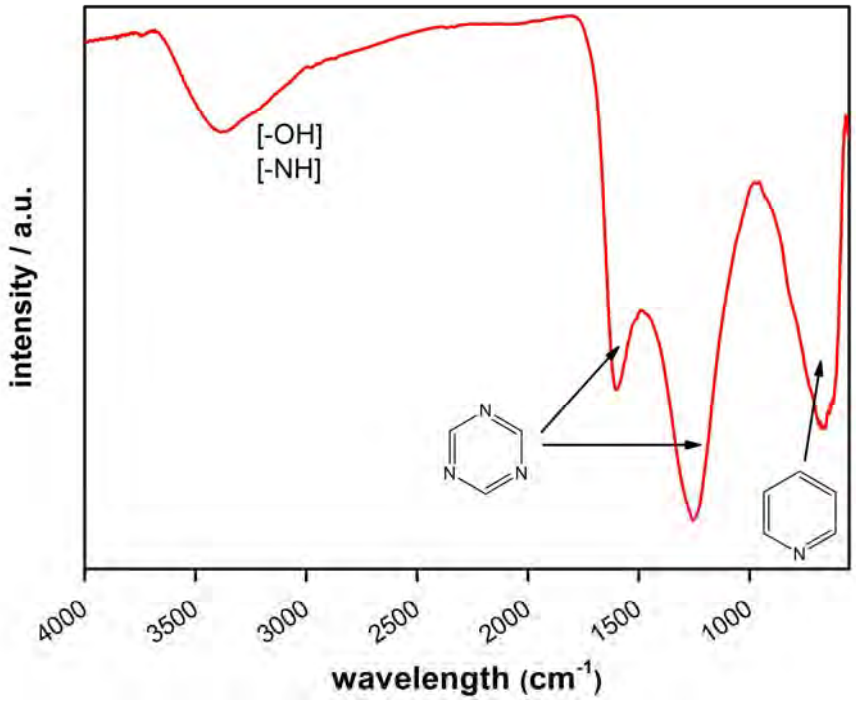

Figure S14. Fourier transform infrared (FT-IR) spectrum of CTF material. The FT-IR spectrum of CTF exhibits characteristic peaks for the expected triazine and pyridine functionalities. However, the broad peak between 3750-2750 cm^{-1} represents (-NH), (-OH) or (-COOH) functionalities, which can possibly be attributed to the acidic hydrolysis of terminal nitrile groups of the CTF scaffold in the course of CTF synthesis procedure.

Solid-state ^{13}C CP-MAS NMR

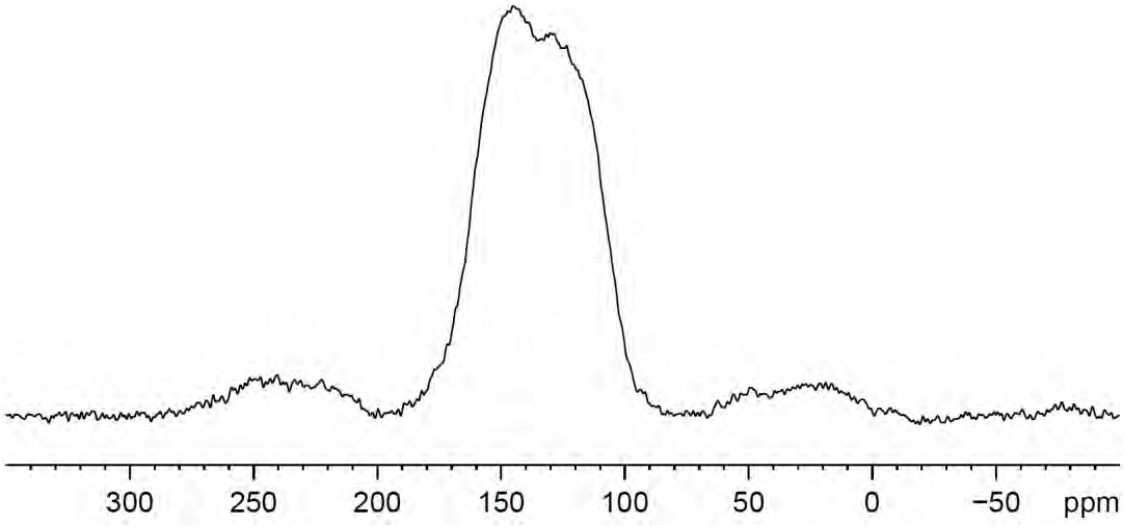

Figure S15. Solid-state ^{13}C NMR analysis of Pt-CTF. The ^{13}C CP-MAS NMR spectrum for Pt-CTF exhibits a broad peak in the range of 100-180 ppm indicating a broad range of carbon species which can be attributed to the high polymerization temperatures of up to 600°C and, thus, to a mild carbonization process leading to the rearrangement of the carbon scaffold. Similar behavior could be observed from the XPS N1s spectra of CTF indicating the presence of additional nitrogen species (other than pyridine nitrogen) which result from thermally induced rearrangement of the CTF network. However, the strong resonances in the range of δ = 90-160 ppm suggest the exclusive presence of aromatic carbon species.